ATMOSPHERIC ENVIRONMENT: X 32 (2026) 100524

Contents lists available at ScienceDirect

Atmospheric Environment: X

journal homepage: www.journals.elsevier.com/atmospheric-environment-x

Continuous fossil fuel CO_2 emission estimates based on ^{14}C-calibrated urban eddy-covariance fluxes of co-emitted species

Ann-Kristin Kunz [a,b,*], Samuel Hammer [b,c], Patrick Aigner [d], Lars Borchardt [e], Jia Chen [d], Julian Della Coletta [b,c], Markus Eritt [e], Ronny Friedrich [f], Xochilt Gutiérrez [e], Rainer Hilland [a,1], Christopher Holst [g], Armin Jordan [e], Natascha Kljun [h], Richard Kneißl [e], Daniel Kühbacher [d], Changxing Lan [g], Junwei Li [d], Betty Molinier [h], Susanne Preunkert [b,c], Andreas Christen [a]

[a] Chair of Environmental Meteorology, University of Freiburg, Werthmannstraße 10, Freiburg, 79085, Germany
[b] Institute for Environmental Physics, Heidelberg University, Im Neuenheimer Feld 229, Heidelberg, 69120, Germany
[c] ICOS Central Radiocarbon Laboratory, Heidelberg University, Berliner Straße 53, Heidelberg, 69120, Germany
[d] Associate Professorship of Environmental Sensing and Modeling, Technical University of Munich, Theresienstraße 90, Munich, 80333, Germany
[e] Max Planck Institute for Biogeochemistry, Kahlaische Straße 4, Jena, 07745, Germany
[f] Curt-Engelhorn-Zentrum Archäometrie gGmbH, D6, Mannheim, 68159, Germany
[g] Institute of Meteorology and Climate Research Atmospheric Environmental Research, Karlsruhe Institute of Technology, Kreuzeckbahnstraße 19, Garmisch-Partenkirchen, 82467, Germany
[h] Department of Earth and Environmental Sciences, Lund University, Sölvegatan 12, Lund, 22362, Sweden

ARTICLE INFO

Keywords:
Carbon dioxide emissions
Fossil fuels
Biogenic flux
Tall-tower eddy covariance
Relaxed eddy accumulation
Emission inventory
Urban environment

ABSTRACT

Atmospheric tall-tower measurements of radiocarbon ($^{14}CO_2$), carbon monoxide (CO), and nitrogen oxides (NO_x) show great potential for determining fossil fuel (ff) CO_2 emissions. While $^{14}CO_2$ relaxed eddy accumulation (REA) enables F_{ffCO_2} estimation during individual hours, F_{CO} and F_{NO_x}, measured directly and continuously by eddy covariance (EC), can be used as proxies for continuous F_{ffCO_2} once local F_{proxy}/F_{ffCO_2} ratios (R_{proxy}) are known. We combined for the first time half-hourly EC F_{CO} and F_{NO_x}, measured along F_{CO_2} at a tall tower in Munich from July 2024 to February 2025, with co-located F_{ffCO_2} from 76 hour-long $^{14}CO_2$ REA measurements. First, we examined the general applicability of CO- and NO_x-based F_{ffCO_2} estimation by analyzing the ^{14}C-based R_{proxy}. Then, we applied the ^{14}C-calibrated $\langle R_{proxy} \rangle$ to the F_{proxy} time series to obtain continuous $ffCO_2$ and non-fossil (nf) CO_2 fluxes, and analyze the F_{CO_2} composition. We demonstrate the potential of the purely observation-based partitioning approach by comparing R_{proxy} and half-hourly F_{ffCO_2} and F_{nfCO_2} with modeled fluxes obtained from a footprint-weighted state-of-the-art Munich emission inventory and biospheric flux model. Although variability in R_{proxy} limits precision and accuracy of half-hourly, proxy-based F_{ffCO_2}, average daytime fluxes could be estimated with about 20% uncertainty. On average, F_{ffCO_2} accounted for 70% of F_{CO_2} during daytime. The absolute modeled F_{ffCO_2} was 46% higher due to increased modeled heating emissions in the cold months. Observation-based and modeled F_{nfCO_2} indicated substantial human respiration and minor biospheric flux contributions. The multi-proxy EC and REA measurements enabled unique analysis and independent evaluation of urban $ffCO_2$ and $nfCO_2$ fluxes.

* Corresponding author at: Chair of Environmental Meteorology, University of Freiburg, Werthmannstraße 10, Freiburg, 79085, Germany.
E-mail addresses: ann-kristin.kunz@meteo.uni-freiburg.de (A.-K. Kunz), shammer@iup.uni-heidelberg.de (S. Hammer), patrick.aigner@tum.de (P. Aigner), lborch@bgc-jena.mpg.de (L. Borchardt), jia.chen@tum.de (J. Chen), jdella@iup.uni-heidelberg.de (J. Della Coletta), meritt@bgc-jena.mpg.de (M. Eritt), ronny.friedrich@ceza.de (R. Friedrich), xgutierrez@bgc-jena.mpg.de (X. Gutiérrez), rainer.hilland@tno.nl (R. Hilland), christopher.holst@kit.edu (C. Holst), ajordan@bgc-jena.mpg.de (A. Jordan), natascha.kljun@mgeo.lu.se (N. Kljun), rkneissl@bgc-jena.mpg.de (R. Kneißl), daniel.kuehbacher@tum.de (D. Kühbacher), changxing.lan@kit.edu (C. Lan), junwei.li@tum.de (J. Li), betty.molinier@mgeo.lu.se (B. Molinier), spreunkert@iup.uni-heidelberg.de (S. Preunkert), andreas.christen@meteo.uni-freiburg.de (A. Christen).
[1] Current affiliation: Netherlands Organisation for Applied Scientific Research (TNO), Environmental Modelling, Sensing, and Analysis, Westerduinweg 3, Petten, Netherlands.

https://doi.org/10.1016/j.aeaoa.2026.100524
Received 3 July 2026; Received in revised form 22 September 2026; Accepted 7 October 2026
Available online 15 October 2026
2590-1621/© 2026 The Authors. Published by Elsevier Ltd. This is an open access article under the CC BY license (http://creativecommons.org/licenses/by/4.0/).
Open access funding enabled and organized by Projekt DEAL.

1. Introduction

Monitoring urban greenhouse gas emissions with high temporal and spatial resolution requires both atmospheric measurements and modeling (e.g., Christen, 2014; Turnbull et al., 2025). State-of-the-art emission inventories provide annual emission estimates for entire cities with a spatial resolution of, e.g., 10 m and a 30 min temporal resolution based on either human activity data and emission factors ("bottom-up") or on nationally reported annual emission data and downscaling proxies ("downscaled"). Atmospheric measurements are usually restricted to smaller spatial and temporal subsets, e.g., several months of collected data covering a certain city district, and only provide aggregated signals from all emission sectors; however, they are crucial for independent validation and refinement of the emission estimates (e.g., Christen, 2014; Chen et al., 2016; Gurney et al., 2017; Stagakis et al., 2023a,b; Brunner et al., 2025). For example, eddy covariance (EC) measurements on urban tall towers can provide direct flux estimates of various greenhouse gases, including carbon dioxide (CO_2), carbon monoxide (CO), nitrogen oxides (NO and NO_2, summarized as NO_x), and methane (CH_4), at the neighborhood scale with a temporal resolution of 30 min (e.g., Feigenwinter et al., 2012; Karl et al., 2017; Hilland et al., 2025b). Using turbulence data and surface characteristics to estimate the source area contributions (flux footprint modeling; e.g., Kljun et al., 2015), the observation-based fluxes can be directly compared to inventory-based flux estimates (e.g., Christen et al., 2011; Wu et al., 2022; Molinier et al., 2026). However, in the case of CO_2, the comparison between observation-based and modeled fluxes is complicated by the fact that emission inventories only account for anthropogenic CO_2 emissions, i.e., primarily emissions from fossil fuel combustion, possibly also emissions from biofuels and human respiration. In contrast, net atmospheric CO_2 measurements include all CO_2 flux contributions, including biospheric fluxes from soil and plant respiration, and photosynthetic uptake. To compare net CO_2 fluxes, biospheric fluxes can be estimated using urban vegetation models (e.g., Stagakis et al., 2025; Li et al., 2026). However, modeling biogenic fluxes involves considerable uncertainties, and comparing net CO_2 fluxes does not allow for independent, separate validation of fossil fuel (ff) and non-fossil (nf) CO_2 fluxes (hereafter referred to as F_{ffCO_2} and F_{nfCO_2}). Independent validation of F_{ffCO_2} requires a partitioning of the observation-based net CO_2 fluxes.

The ideal tracer for separating $ffCO_2$ and $nfCO_2$ is radiocarbon (^{14}C), which is commonly denoted in Δ-notation according to Stuiver and Polach (1977). Due to its radioactive decay with a half-life of 5730 yr, millions of years old fossil fuels are depleted of ^{14}C, and their combustion dilutes the natural atmospheric $^{14}C/^{12}C$ ratio. Consequently, low atmospheric $^{14}C/^{12}C$ ratios indicate large CO_2 contributions from $ffCO_2$ emissions (e.g., Levin et al., 2003; Turnbull et al., 2016; Maier et al., 2023). While $^{14}CO_2$ EC measurements have not yet been possible due to the lack of accurate, fast-response gas analyzers for $^{14}CO_2$, relaxed eddy accumulation (REA) measurements for $^{14}CO_2$ enable a purely observation-based estimation of $ffCO_2$ fluxes (Kunz et al., 2025b, 2026a). However, due to the labor and logistical requirements associated with $^{14}CO_2$ measurements, REA $ffCO_2$ fluxes can only be determined for a limited number of discrete sampling periods (Kunz et al., 2025b).

To obtain continuous $ffCO_2$ fluxes, EC CO and NO_x fluxes show great potential. Both CO and NO_x fluxes are proxies for $ffCO_2$ emissions, because both gases are co-emitted with $ffCO_2$ during the combustion of fossil fuels. They are therefore referred to as F_{proxy} in the following. However, the F_{proxy}/F_{ffCO_2} ratio varies depending on the fuel carbon content and combustion conditions (Turnbull et al., 2015; Rosendahl, 2022; Maier et al., 2024a). Consequently, different source sectors, e.g., stationary combustion and road transport, have significantly different emission ratios. Moreover, a large variability within the source sectors has been reported (Karl et al., 2017; Rosendahl, 2022). Due to regional differences, e.g., in fleet composition and heating types, F_{proxy}/F_{ffCO_2} ratios are site-specific (Rosendahl et al., 2022). Consequently, accurate, proxy-based determination of continuous $ffCO_2$ fluxes requires knowledge of the temporally varying local F_{proxy}/F_{ffCO_2} ratios. Due to the lack of direct observations of F_{proxy}/F_{ffCO_2} ratios and their temporal variability, different proxy-based approaches have been applied to partition net CO_2 fluxes. Hilland et al. (2025b) considered average F_{CO}/F_{CO_2} and F_{NO_x}/F_{CO_2} ratios obtained for the sectors stationary combustion and road transport from a city inventory in a $4 \times 4\,km^2$ square centered at the 112 m high EC tower in the city of Zurich. However, improbable and impossible results for some cardinal directions and some times of the day indicated that using constant, inventory-based emission ratios was not appropriate for CO_2 flux partitioning. Wu et al. (2022) used a constant F_{CO}/F_{ffCO_2} ratio, which was determined from differences in molar mixing ratios between upwind and downwind flask samples. However, applying ratios of concentration differences to turbulent flux measurements implicitly assumes that the concentration footprint is representative of the flux footprint, which is generally not the case in a heterogeneous urban environment. Similar approaches were used with excess concentrations, considering a clean background concentration (Δc). Turnbull et al. (2015), Maier et al. (2024a), and Juchem et al. (2025), for example, used average $\Delta c_{proxy}/\Delta c_{ffCO_2}$ ratios obtained from flask concentration measurements to calculate continuous proxy-based Δc_{ffCO_2} time series. The Δc_{ffCO_2} record can be used to estimate urban $ffCO_2$ fluxes, but this method relies on the use of inversion models (Maier et al., 2024b). While the aforementioned studies justified the use of a constant proxy/$ffCO_2$ ratio based on sufficiently high correlations between observed proxy and $ffCO_2$ excess concentrations and small or no temporal or spatial differences, its applicability to direct flux measurements has not yet been investigated, to our knowledge.

In this study, we use REA $^{14}CO_2$ and EC CO and NO_x observations taken at a tall tower in the city of Munich between July 2024 and March 2025, a Munich emission inventory, a Vegetation Photosynthesis and Respiration Model (VPRM), and modeled flux footprints to investigate the composition of urban CO_2 fluxes and to compare different methodological approaches. The study consists of three parts:

- First of all, we analyze purely observation-based F_{proxy}/F_{ffCO_2} ratios from 76 hour-long REA $^{14}CO_2$ and co-located EC CO and NO_x measurements to address the general applicability of proxy-based $ffCO_2$ flux estimation in an urban environment. For this purpose, we evaluate the correlations between F_{CO} and F_{NO_x} with F_{ffCO_2} and their dependence on air temperature and wind direction (Sections 3.1, 4.1, and 4.2). We also analyze the similarities and differences between the two proxies, and discuss the resulting uncertainties in the proxy-based F_{ffCO_2}.
- We then apply the ^{14}C-calibrated F_{proxy}/F_{ffCO_2} ratios from the REA measurements to the continuous EC proxy fluxes to obtain a continuous, purely observation-based F_{ffCO_2} time series at 30 min temporal resolution (Section 3.2). Based on the CO- and NO_x-based F_{ffCO_2} time series, we investigate the average contributions of fossil and non-fossil CO_2 fluxes to net EC CO_2 fluxes measured at the Munich tall tower (Section 4.3).
- In both steps, we compare our observation-based F_{proxy}/F_{ffCO_2} ratios and the observation-based, continuous F_{ffCO_2} and F_{nfCO_2} time series with modeled fluxes and flux ratios obtained by convolving a state-of-the-art Munich emission inventory (Dröge et al., 2024; Kühbacher et al., 2025, 2026b; Aigner et al., 2026) and a VPRM model set up for the city of Munich (Li et al., 2026) with flux footprints that were calculated for a $15 \times 15\,km^2$ area around the measurement site at a 10 m spatial resolution and 30 min temporal resolution (Molinier and Kljun, 2024). Since both observation- and model-based approaches to estimating F_{ffCO_2} and F_{nfCO_2} are subject to substantial uncertainties, this comparison enables a first independent evaluation of both approaches and lays the foundation for future methodological improvements.

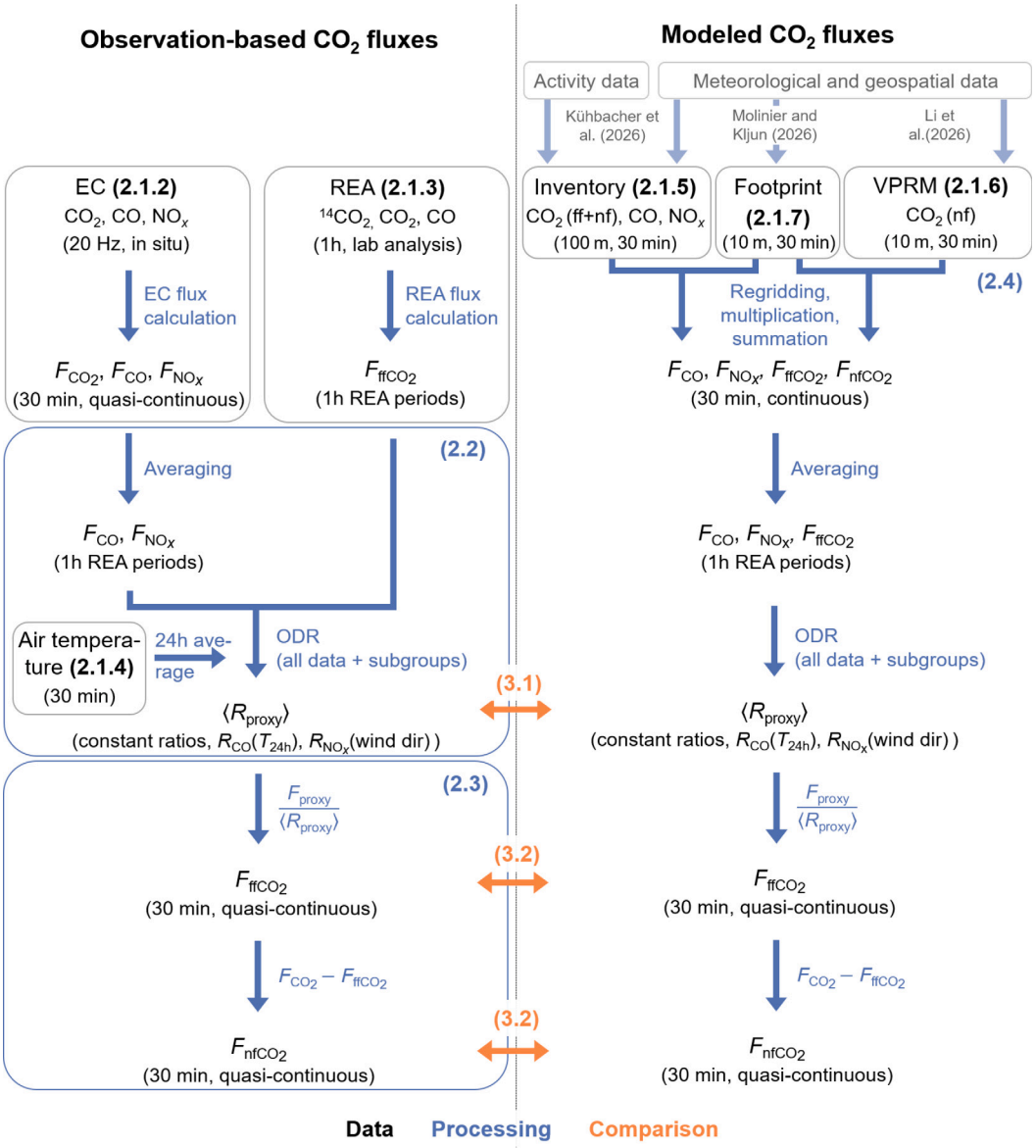


Fig. 1. Overview of the methodological approach used to estimate fossil fuel (ff) and non-fossil (nf) CO_2 fluxes based on eddy covariance (EC) and relaxed eddy accumulation (REA) measurements. $\langle R_{proxy} \rangle$ denotes the average F_{proxy}/F_{ffCO_2} ratio obtained through an orthogonal distance regression (ODR). The modeled fluxes are based on a state-of-the-art emission inventory for the city of Munich, a high-resolution Vegetation, Photosynthesis, and Respiration Model (VPRM) for the Munich area, and flux footprints modeled for the EC measurements in Munich, which have been described in detail in Kühbacher et al. (2026b), Li et al. (2026), and Molinier and Kljun (2024), respectively. Bold numbers in parentheses denote the sections in which the data, processing, and comparison of observation-based and modeled flux estimates are described.

This study was conducted within the ICOS (Integrated Carbon Observation System) Cities project, a Horizon 2020 project funded by the European Union to implement and evaluate greenhouse gas measurement methodologies and services for cities in order to support climate action.

2. Methods

Estimating $ffCO_2$ and $nfCO_2$ fluxes at a half-hourly resolution and comparing them with modeled flux estimates involves several data sets and methodological steps (Fig. 1). Section 2.1 describes the measurement site and data sets, while Sections 2.2–2.4 explain the data processing and analysis.

2.1. Site and data description

2.1.1. Munich flux tall tower

Flux measurements were conducted on an active telecommunications tower located near the city center of Munich, Germany (48° 8′50.9″N, 11° 32′59.3″E, 85 m above ground level, ICOS Station ID DE-Opd). Munich is the largest city and capital of Bavaria, with approximately 1.6 million inhabitants as of 2024 (Statistisches Amt München, 2026). The inner-city area is located alongside the River Isar and comprises a variety of residential and office buildings (mostly multi-family buildings connected to a district heating system; Aigner et al., 2026), a historical old town, the central railway station and several parks. The inner city is surrounded by the middle ring, which experiences heavy traffic. The outskirts are characterized by single-family and semi-detached houses that are predominantly heated by natural gas (Aigner

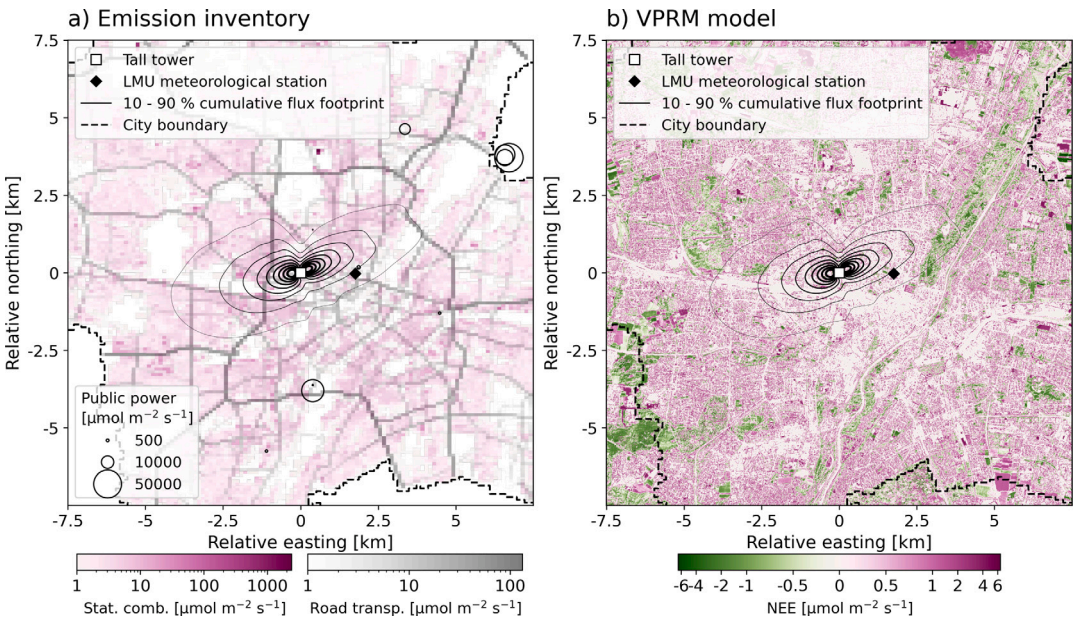


Fig. 2. Location of the tall tower and cumulative flux footprint of the continuous, quality-controlled, closed-path EC CO_2 flux measurements according to Kljun et al. (2015). The depicted areas contributed an average of 10 %–90 % to the turbulent fluxes at the measurement site (Section 2.1.7). The base map shows for a 15 × 15 km^2 area centered around the measurement site (a) the mean annual CO_2 emissions from road transport, stationary combustion, and public power in 2024 according to the Munich emission inventory (Section 2.1.5), and (b) the mean annual net ecosystem exchange (NEE), according to a high-resolution VPRM model for 2024 (Section 2.1.6). Inventory data is only available within the administrative boundary of the City of Munich. Air temperature and radiation measurements used in this study were taken at the meteorological station of the Ludwig-Maximilian University (LMU).

et al., 2026), as well as several large green areas, such as the English Garden, the Botanical Garden, and the Olympia Park. Deciduous trees dominate evergreens (Li et al., 2026). Several combined heat and power plants within the administrative city boundary supply the district heating network (Aigner et al., 2026). The measurement site was located approximately 2 km northeast of the historical city center, and 1 km northeast of the central railway station, within the middle ring (Fig. 2). The 80 % flux footprint encompassed an area that was usually well within a 15 × 15 km^2 area centered on the flux tower (Fig. 2, Section 2.1.7). Atmospheric flux measurements were most influenced by processes in the city center, but could also contain signals from the middle ring and beyond. At 10 m gridded scale, about 60 % of this area is covered by buildings (mostly residential buildings), about 30 % by vegetation, and about 10 % by roads, railways, and other land cover types. In all cardinal wind directions, the vegetated surface area fraction increases with distance from the tower. In a 5 × 5 km^2 area centered on the tower, the fraction of built-up and vegetated area is approximately 54 % and 28 % west of the tower, and 71 % and 16 % east of the tower, respectively. The tower itself is 59 m high and has a 42 m antenna on top. On the antenna, a horizontal boom with an anemometer, an open-path gas analyzer, and gas inlets for a closed-path gas analyzer and flask measurements was mounted. The boom was approximately 1.2 m long and oriented towards the south at a height of 85 m above ground level. Further information on the measurement site, including a photo of the tower and a detailed analysis of flow distortion effects, can be found in Lan et al. (2024) and Kunz et al. (2026a).

2.1.2. *Continuous eddy covariance measurements (F_{CO_2}, F_{CO}, F_{NO_x})*

From July 2024 to March 2025, two EC gas analyzers were operated at the Munich flux tall tower: an open-path CO_2/H_2O gas analyzer integrated into a 3D sonic anemometer (IRGASON, Campbell Scientific, Inc., Logan, UT, USA), which measured CO_2, H_{20}, and 3D turbulence at a frequency of 20 Hz, and a closed-path multicompound gas analyzer (MGA^7, MIRO Analytical AG, Wallisellen, Switzerland), which measured CO_2, CO, NO, NO_2, H_2O, CH_4, and N_2O at a frequency of 10 Hz using four lasers for mid-infrared quantum cascade laser spectroscopy (Hilland et al., 2025b). Due to a laser failure of the MGA^7 in March 2025, EC measurements from the MGA^7 were only available until the end of February 2025. Based on the high-frequency EC measurements of the MGA^7, we calculated CO_2, CO, NO, and NO_2 turbulent fluxes using the EddyPro software (v7.0.9, Li-COR Biosystems) with an averaging period of 30 min (Lan et al., 2024) and common EC processing options for urban flux measurements. As NO and NO_2 are quickly converted into each other, we considered the sum of the two fluxes (NO_x) for further analysis. The average normalized spectra and co-spectra of all gases showed sufficient agreement with theoretical expectations (Fig. A.13), indicating good quality of the EC flux results. The good quality of the MGA^7 CO_2 fluxes was also demonstrated by their good agreement with the IRGASON CO_2 fluxes (Appendix A). Due to the greater data availability and consistency with the CO and NO_x measurements by the MGA^7, the MGA^7 CO_2 fluxes rather than the IRGASON CO_2 fluxes were considered in this study. For details on the EC data processing, see Appendix A, Hilland et al. (2025b), and Kunz et al. (2026a).

For quality control purposes, we applied common EC filters, as well as site-specific flagging criteria. For example, we excluded unusually high CO fluxes from the southeast as these were not captured by the REA measurements (Appendix A). In addition, we only considered data from working days (Section 2.1.3) and data for which quality-controlled flux footprints were available (Section 2.1.7). After quality control, 3017 half-hourly flux measurements (26 %) from working days with quality-controlled footprint data were available (Table A.4, Fig. 3b). The retained flux measurements with quality-controlled footprint data were representative of the total number of quality- controlled EC data during working days. On average, 20 EC flux data points were retained per hour between 07:00 and 20:00 local time (LT = UTC + 2 during Central European Summer Time and UTC + 1 during Central European Winter Time), and 10 per hour between 20:00 and 07:00 LT (Fig. 3b).

During the half-hourly timestamps with quality-controlled EC and footprint data, the wind predominantly blew from the northeast-east or southwest-west (Fig. 4). The observed wind statistics were representative of the prevailing wind conditions in Munich.

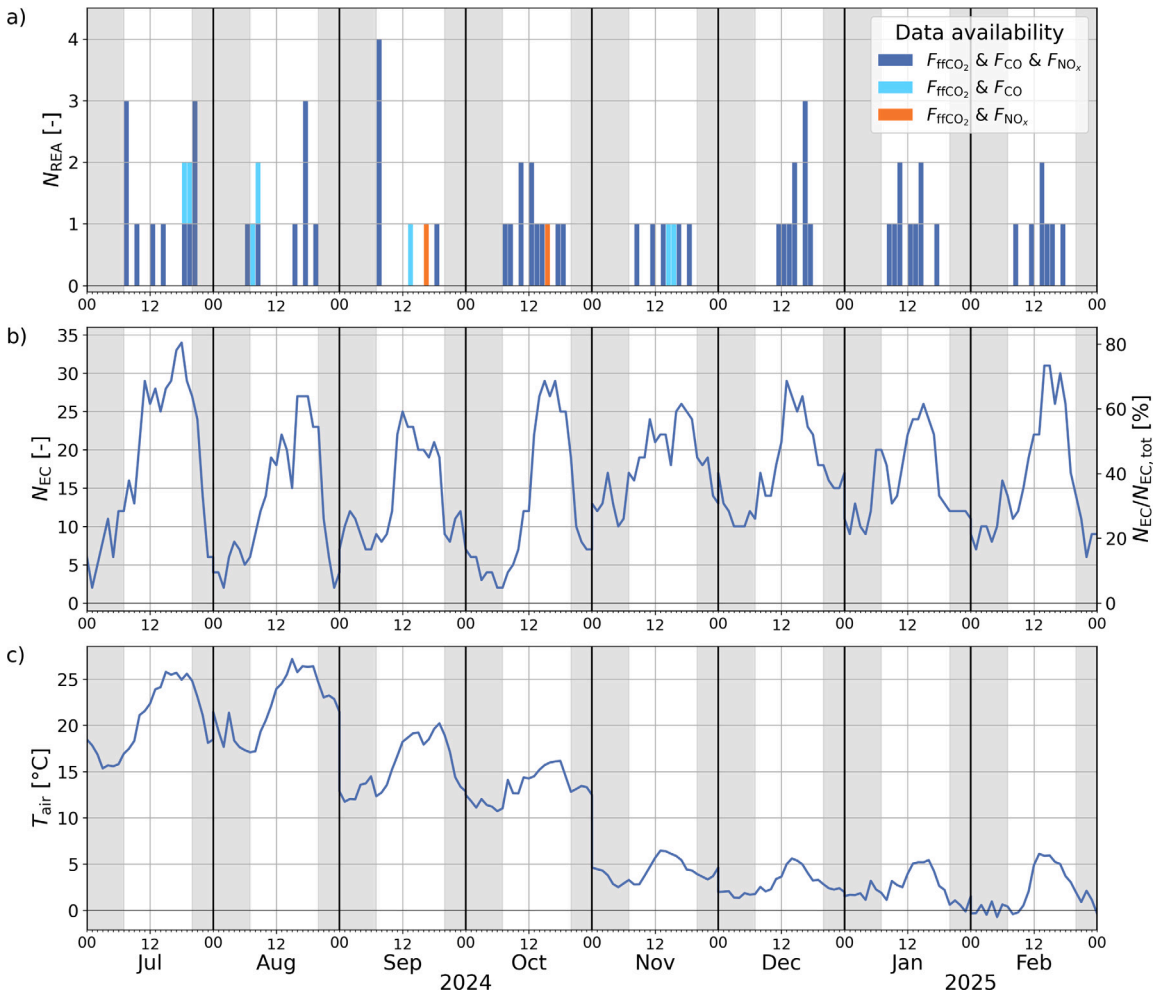


Fig. 3. (a) Number of F_{ffCO_2} REA measurements N_{REA} with concurrent, quality-controlled F_{CO} and/or F_{NO_x} measurements. Six REA measurements with flask-based F_{CO} and F_{ffCO_2} were taken in March 2025 but are not shown in the figure, as EC measurements were only available until the end of February 2025 due to a laser failure of the MGA[7] in March 2025 (Section 2.2). (b) Number N_{EC} and percentage $N_{EC}/N_{EC,\ tot}$ of EC measurements that passed the quality control tests for CO_2, CO, and NO_x for each hour of the day (only working days) and month. The percentage of measurements is based on an average of 21.125 working days per month, meaning $N_{tot} = 42.25$ half-hourly flux values correspond to 100 % for each hour of the day. (c) Mean air temperature T_{air} during the 30 min periods with quality-controlled EC flux data.

2.1.3. *Discrete relaxed eddy accumulation measurements (F_{ffCO_2})*

In addition to continuous EC flux measurements, REA measurements for ^{14}C-based $ffCO_2$ flux estimation were conducted during daytime on working days, usually every other hour when there was no precipitation. No REA measurements were taken on weekends, public holidays, or at night because the limited number of REA flask samples that could be analyzed in the laboratory (for logistical and financial reasons) would not have been sufficient to resolve the systematic differences in anthropogenic emissions compared to weekday daytime. In addition, suppressed turbulence limits REA measurements at night (Fotiadi et al., 2005). The REA flask sampling system, the ^{14}C-based estimation of $ffCO_2$ concentration differences and $ffCO_2$ fluxes, as well as the collection, quality control, and flagging of the REA measurements in Munich are briefly summarized below, while detailed descriptions can be found in Kunz et al. (2025b, 2026a).

During the hour-long REA measurement periods, air was conditionally collected in separate updraft and downdraft reservoirs based on the 20 Hz vertical wind velocity from the 3D sonic anemometer. To increase the concentration differences between the updraft and downdraft samples, air was rejected during periods of low vertical wind. This so-called "deadband" was defined as $1.1\sigma_w$, where the standard deviation of the vertical wind velocity σ_w was determined from the preceding 30 min time period. For seven REA measurements conducted in July, August, and September, when surface emissions were expected to be small, hyperbolic REA with a "hole size" H of 0.8 was applied to further increase the concentration difference between the updraft and downdraft samples (Kunz et al., 2026a). After the sampling periods, the collected air was transferred to glass flasks. Based on suitable micrometeorological conditions, 99 updraft and downdraft flask sample pairs were selected for laboratory analysis (Kunz et al., 2026a). The selected flask pairs were analyzed, for CO_2, CO, and other gases at the ICOS Flask and Calibration Laboratory in Jena, Germany, and for $^{14}CO_2$ at the ICOS Central Radiocarbon Laboratory in Heidelberg, Germany. Based on the CO_2 and ^{14}C-based $ffCO_2$ concentration differences between updraft and downdraft flask samples (ΔCO_2 and $\Delta ffCO_2$, respectively) and the average CO_2 fluxes measured during the REA sampling period by EC (F_{CO_2}), $ffCO_2$ fluxes were calculated according to Eq. (1) (Kunz et al., 2025b).

^{14}C-based F_{ffCO_2}:

$$F_{ffCO_2} = \beta\, \sigma_w\, \overline{\rho_m}\, \Delta ffCO_2 = \frac{F_{CO_2}}{\Delta CO_2}\, \Delta ffCO_2. \quad (1)$$

σ_w is the standard deviation of the vertical wind velocity, $\overline{\rho_m}$ is the mean molar density of dry air, and β is a proportionality factor. $\beta\, \sigma_w\, \overline{\rho_m}$ was determined for each REA measurement period based on ΔCO_2 and F_{CO_2}. After final quality control, the dataset included 76 hours

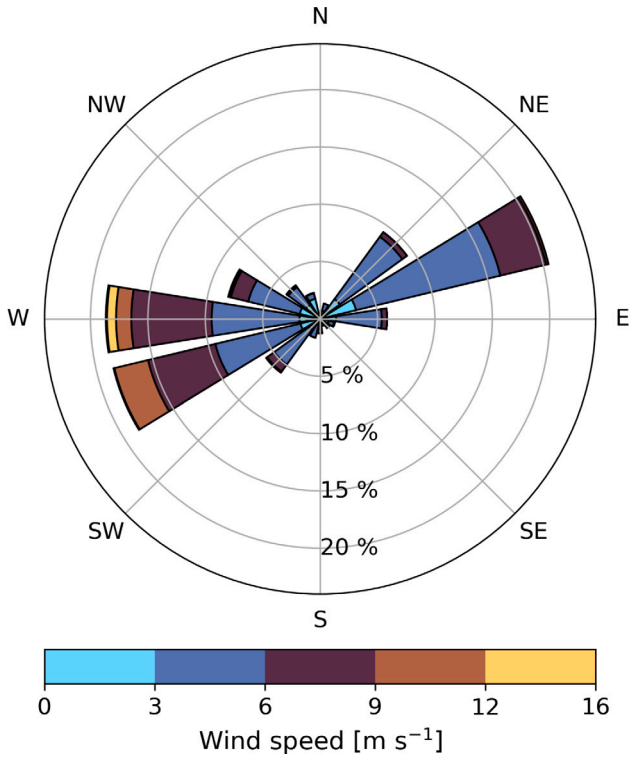


Fig. 4. Frequency of counts by horizontal wind direction and wind speed measured by the 3D sonic anemometer for all 30 min flux measurement periods that passed the quality control tests and for which footprint data are available (N = 3017). Measurements with wind direction >340°N or <20°N were removed due to flow distortion effects.

with good-quality $ffCO_2$ and CO flux observations, and 65 hours with $ffCO_2$ and NO_x flux observations. For these measurements, the CO_2 quality control flag according to Mauder and Foken (2004) was <2, the friction velocity u_* was >0.2 m s^{-1}, the absolute CO_2 storage flux was <20 μmol m^{-2} s^{-1}, the β-coefficient was between 0.1 and 1, and the minimum of the relative $ffCO_2$ and $nfCO_2$ flux uncertainties was <100 % (Kunz et al., 2026a). Unlike the EC fluxes, the REA $ffCO_2$ fluxes could not be corrected for changes in storage below the measurement height. However, since measurements from periods with large storage fluxes were excluded, storage fluxes can be considered negligible (Kunz et al., 2026a). Since REA measurements were only conducted during daytime on working days (Fig. 3a), and differences between day and night, as well as between working days and weekends or public holidays, could not be resolved, we primarily focus on the time period between 07:00 and 20:00 LT on working days.

2.1.4. Continuous air temperature and radiation measurements

To analyze how the flux measurement results depended on ambient air temperature and shortwave downwelling radiation, we used continuous temperature and radiation measurements conducted by the Meteorological Institute of the Ludwig-Maximilian University (LMU) in Munich. The measurement station ("Stadtstation", ID MIM01) is located approximately 2 km east of the flux tower (Fig. 2). Air temperature was measured 30 m above ground level. For 67 half-hourly time periods without temperature data from the LMU station, we used air temperature measurements from the IRGASON. To account for the 55 m height difference and any minor instrument differences between the two temperature sensors, we added the average observed offset of 1 °C to the IRGASON measurements.

2.1.5. Munich emission inventory (F_{CO_2}, F_{CO}, F_{NO_x})

A gridded emission inventory, developed as part of the ICOS Cities project, provided flux estimates of CO_2 (distinguishing between fossil and non-fossil CO_2), CO, and NO_x within the administrative borders of the city of Munich in 2024 and 2025, with a spatial resolution of 1/600° × 1/1200° (approximately 100 m × 100 m) and an hourly temporal resolution (Aigner et al., 2025; Kühbacher et al., 2026b). The inventory is a combined product of bottom-up estimates for the Gridded Nomenclature For Reporting (GNFR) sectors of public power (GNFR A), stationary combustion (GNFR C), road transport (GNFR F), and human respiration, developed by the Technical University of Munich (TUM), and a spatially downscaled regional inventory for the remaining sectors, provided by the Netherlands Organization for Applied Scientific Research (TNO). For the bottom-up estimation, as well as for the spatial downscaling, activity data (e.g., fuel input and traffic counting data), meteorological data (e.g., air temperature), and geospatial data (e.g., land cover maps), were used (Fig. 1). In this study, we used Version 2.6.0 of the emission inventory. The emissions of the road transport sector were estimated using HBEFA (Handbook Emission Factors for Road Transport) emission factors, Version 5.107 (Notter et al., 2026). For comparison, we present results from a previous version of the emission inventory, which used HBEFA 4.2 emission factors (Notter et al., 2022) for the road transport sector, as presented in Kühbacher et al. (2025) (Appendix F). The bottom-up sectors covered 97 % of the annual CO_2 emissions, 93 % of the annual NO_x emissions, and 71 % of the annual CO emissions in the inventory. The annual mean CO_2 emissions from road transport and stationary combustion, as well as point-source emissions from the public power sector are shown in Fig. 2a. These three source sectors were the major contributors to the annual anthropogenic CO_2 emissions within a 15 × 15 km^2 area centered on the measurement site. The relative contributions of all source sectors to the annual CO_2, CO, and NO_x emissions are provided in Appendix E. For detailed descriptions of the bottom-up approaches for stationary combustion, public power, and road transport, as well as of the downscaling of the other sectors and estimation of human respiration, we refer to Aigner et al. (2026), Kühbacher et al. (2025), and Dröge et al. (2024).

2.1.6. VPRM model (NEE)

Net ecosystem exchange (NEE), i.e., biospheric net CO_2 fluxes, were modeled for the entire measurement period and the entire 15 × 15 km^2 domain using a biospheric CO_2 flux estimation framework with 10 m spatial and hourly temporal resolution developed by Li et al. (2026). This fine-scale biospheric model is based on the Vegetation Photosynthesis and Respiration Model (VPRM). The model was driven by air temperature at a height of 2 m above ground level and shortwave downward solar radiation at the surface measured at the meteorological station "Stadtstation" of the LMU (Fig. 2, Section 2.1.4), as well as by the Enhanced Vegetation Index (EVI) and the Land Surface Water Index (LSWI) derived from the Sentinel-2 multispectral imaging satellite with a spatial resolution of 10 m. The annual average NEE was slightly positive in the built-up area and slightly negative in the highly vegetated area, e.g., along the River Isar (Fig. 2b). Further details on the VPRM model can be found in Li et al. (2026).

2.1.7. Flux footprints

The source area contributions to the turbulent flux measurements (in m^{-2}) were derived as part of the ICOS Cities project for a 15 × 15 km^2 area centered at the measurement site using the Flux Footprint Prediction (FFP) by Kljun et al. (2015) (Molinier and Kljun, 2024). The gridded flux footprint functions (here denoted as "flux footprints") have a spatial resolution of 10 m and temporal resolution of 30 min. For the FFP, roughness length and displacement height were derived from building and vegetation height maps (Molinier et al., 2026). Boundary layer heights were obtained from the ERA5 reanalysis estimates from the Copernicus Climate Change Service (Hersbach et al., 2023), and

turbulence data were taken from the open-path EC measurements (ICOS Ecosystem Thematic Centre et al., 2025). Since meaningful EC measurements require well-developed turbulence, footprints were only calculated for 30 min time periods with a friction velocity of $u_* > 0.2\,\mathrm{m\,s^{-1}}$ and with data that passed the integrated turbulence characteristics test according to Foken et al. (2004). To avoid conditions with potential decoupling between the measurement height and the surface, we removed data from periods when the boundary layer height was below 105 m (measurement height+20 m), as suggested in Molinier and Kljun (2024). Furthermore, due to the finite size of the modeled footprint, we only considered periods for which at least 80 % of the observation-based flux originated from within the $15 \times 15\,\mathrm{km^2}$ area. For details on the flux footprint modeling, see Molinier and Kljun (2024) and Molinier et al. (2026).

2.2. Calculation of observation-based $F_{\mathrm{proxy}}/F_{\mathrm{ffCO_2}}$ ratios ($\langle R_{\mathrm{proxy}}\rangle$)

To calculate the average $F_{\mathrm{proxy}}/F_{\mathrm{ffCO_2}}$ ratio from the REA and EC measurements, we first determined the average proxy fluxes (i.e., F_{CO} and F_{NO_x}) during the individual hour-long REA measurement periods from the 30 min MGA[7] flux data. For further analysis, we only considered measurement periods in which both 30 min proxy fluxes passed the EC quality control. For the final six REA measurements taken in March 2025, we estimated F_{CO} based on CO molar mixing ratios measured in the REA flask samples (Appendix B). These flux estimates have larger uncertainties; however, the additional data were considered more important, given the small overall number of REA measurements. In contrast to CO, NO_x is highly reactive and cannot be measured in flask samples. Therefore, the flask-based calculation of F_{proxy} was only possible for CO.

For the measurement periods with good-quality F_{proxy} and $F_{\mathrm{ffCO_2}}$ data, we then determined the average $F_{\mathrm{proxy}}/F_{\mathrm{ffCO_2}}$ ratio using a weighted total least-squares regression. This regression is a special case of an orthogonal distance regression (ODR) and considers uncertainties in both variables. In our case, the weights were determined as $1/\delta F^2$, where δF is the measurement uncertainty of F_{proxy} or the $F_{\mathrm{ffCO_2}}$. Following Maier et al. (2024a), the slope of this linear regression provides a bias-free average flux ratio, in the following denoted as $\langle R_{\mathrm{proxy}}\rangle$. To analyze the variability of R_{proxy}, average ratios were also determined for subgroups of REA measurement periods depending on various variables such as the average wind direction and the average air temperature. In this case, $\langle R_{\mathrm{proxy}}\rangle$ is a function of wind direction or air temperature (Eq. (2), Appendix C). A temperature-driven change in the relative contribution of stationary combustion to the total CO_2 emissions, and thus in R_{proxy}, may depend not only on the current air temperature but also on the average temperature of the recent past. Therefore, we also considered the average air temperatures 24 h prior to the start of the measurement, denoted as $T_{24\mathrm{h}}$.

$$\langle R_{\mathrm{proxy}}\rangle = \langle \frac{F_{\mathrm{proxy}}}{F_{\mathrm{ffCO_2}}} \rangle = \begin{cases} \text{constant} \\ f(T_{24\mathrm{h}}) \\ f(\text{wind direction}) \end{cases} \tag{2}$$

A parameterization of $\langle R_{\mathrm{proxy}}\rangle$ on $T_{24\mathrm{h}}$ was possible for CO, whereas R_{NO_x} showed a larger dependence on the horizontal wind direction. Assuming that there were no significant non-fossil CO or NO_x fluxes within the flux footprint, we forced the ODR through the origin. Known photochemical reactions affecting CO or NO_x mixing ratios can be assumed to be negligible over short time scales between emission and measurement (Lee et al., 2015; Vaughan et al., 2016; Hilland et al., 2025b). However, when the ODR is forced through the origin, the fitted line does not necessarily pass through the centroid of the data, as this property only holds when the intercept is estimated freely. When calculating average, proxy-based $\mathrm{ffCO_2}$ fluxes, we therefore considered an additional uncertainty contribution due to the fit through the origin (Section 2.3).

2.3. Construction of continuous $F_{\mathrm{ffCO_2}}$ and $F_{\mathrm{nfCO_2}}$ time series and estimation of uncertainties

To obtain a quasi-continuous $F_{\mathrm{ffCO_2}}$ time series with a temporal resolution of 30 min, we divided the quality-controlled EC proxy flux data by $\langle R_{\mathrm{proxy}}\rangle$ (Eq. (3)). Using $\langle R_{\mathrm{CO}}\rangle$, $\langle R_{\mathrm{CO}}\rangle(T_{24\mathrm{h}})$, $\langle R_{\mathrm{NO}_x}\rangle$, and $\langle R_{\mathrm{NO}_x}\rangle$(wind direction) we obtained two CO-based and two NO_x-based $F_{\mathrm{ffCO_2}}$ records. We calculated non-fossil CO_2 fluxes as the difference between the net EC CO_2 fluxes measured by the MGA[7] and the proxy-based $\mathrm{ffCO_2}$ fluxes (Eq. (4)).

Proxy-based $F_{\mathrm{ffCO_2}}$ using ^{14}C-calibrated $\langle R_{\mathrm{proxy}}\rangle$:

$$F_{\mathrm{ffCO_2}} = \frac{F_{\mathrm{proxy}}}{\langle R_{\mathrm{proxy}}\rangle} \tag{3}$$

$$F_{\mathrm{nfCO_2}} = F_{\mathrm{CO_2}} - F_{\mathrm{ffCO_2}} \tag{4}$$

Note that the $F_{\mathrm{ffCO_2}}$ calculated from half-hourly EC proxy measurements and ^{14}C-calibrated $F_{\mathrm{proxy}}/F_{\mathrm{ffCO_2}}$ ratios (Eq. (3)) differs from the $F_{\mathrm{ffCO_2}}$ calculated directly from the $^{14}CO_2$ measurements for the REA sampling periods (Eq. (1)). We refer to these as "proxy-based" or "^{14}C-based" $F_{\mathrm{ffCO_2}}$. In general, the $F_{\mathrm{ffCO_2}}$ estimates used to analyze R_{proxy} (Section 3.1) were calculated from Eq. (1), while the continuous $F_{\mathrm{ffCO_2}}$ estimates (Section 3.2) were calculated from Eq. (3). As the calculation is always clear from the context, we do not use different symbols to improve readability. There are several sources of uncertainty in the calculation of $F_{\mathrm{ffCO_2}}$ (Eq. (3)):

(a) The assumption of a constant or temperature-/wind direction-dependent $\langle R_{\mathrm{proxy}}\rangle$ does not capture the temporal variability in R_{proxy} at the measurement site, which is caused by the variability in the source sector contributions and their emission ratios, and by measurement uncertainties.
(b) $\langle R_{\mathrm{proxy}}\rangle$ determined from the limited number of REA measurements may differ from the "true" average ratio of all 30 min time steps. By definition, a sampling bias in $\langle R_{\mathrm{proxy}}\rangle$ will cause the same relative bias in the $F_{\mathrm{ffCO_2}}$ time series.
(c) Average $\mathrm{ffCO_2}$ fluxes include an uncertainty component from the forcing of the ODR through the origin, which does not conserve averages.

To estimate the magnitudes of the uncertainty components (a), (b), and (c), we calculated the root-mean-square deviation (RMSD) between ^{14}C-based and proxy-based $\mathrm{ffCO_2}$ flux estimates during the REA periods, compared observation-based and modeled $\langle R_{\mathrm{proxy}}\rangle$, and conducted a synthetic data experiment, where we considered all three uncertainty components by simulating the observation-based approach and assuming the inventory-based fluxes as the "truth" (Appendix D). Following Maier et al. (2024a), we also estimated the contributions of measurement uncertainties and unaccounted variability in R_{proxy} to the RMSD between ^{14}C-based and proxy-based $\mathrm{ffCO_2}$ flux. To compare the RMSD of the observation-based fluxes with the RMSD between the modeled $F_{\mathrm{ffCO_2}}$ and modeled $F_{\mathrm{proxy}}/\langle R_{\mathrm{proxy}}\rangle$, we computed the normalized RMSD (NRMSD) by dividing the RMSD by the mean $F_{\mathrm{ffCO_2}}$. Details and results of the synthetic data experiments and uncertainty estimation are described in Appendix D.

2.4. Modeling of inventory-based $F_{\mathrm{ffCO_2}}$, $F_{\mathrm{nfCO_2}}$, F_{CO}, F_{NO_x}, and flux ratios

To estimate the CO, NO_x, $\mathrm{ffCO_2}$, and $\mathrm{nfCO_2}$ fluxes that would be measured at the tower according to the emission inventory and the VPRM model, we convolved the Munich emission inventory (Section 2.1.5) and the VPRM model results (Section 2.1.6) with the modeled flux footprint functions (Section 2.1.7) for each 30 min time step as in Molinier et al. (2026). To this end, we converted the unit of the inventory fluxes from $\mathrm{kg\,cell^{-1}\,year^{-1}}$ to $\mu\mathrm{mol\,m^{-2}\,s^{-1}}$ and interpolated

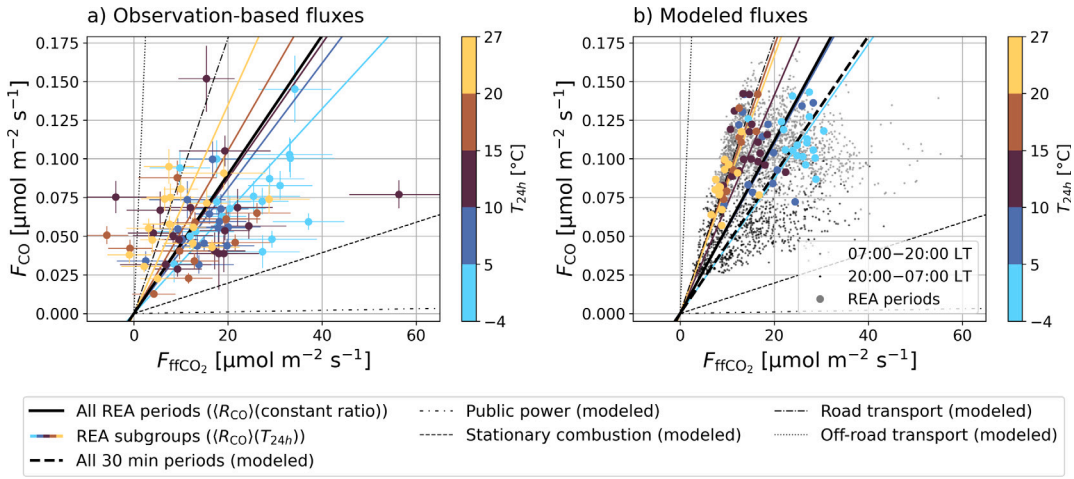


Fig. 5. (a) Observation-based F_{CO} and ^{14}C-based F_{ffCO_2} during the REA sampling periods. The colors indicate the mean air temperatures 24 h prior to the start of the REA sampling (T_{24h}). Solid lines illustrate the orthogonal distance regressions (ODR) for all data points and the respective temperature-based subgroups. For reference, the slopes of the dashed lines represent the average flux ratios of the dominant source sectors obtained from the footprint-averaged emission inventory. (b) Modeled F_{CO} and F_{ffCO_2} at the measurement site for all 30 min timestamps of the EC measurements between 07:00 and 20:00 LT (gray) and between 20:00 and 07:00 LT (black), as well as for the 60 min REA sampling periods (colored circles). For clarity, individual data points with modeled F_{ffCO_2} up to 140 µmol m^{-2} s^{-1} were omitted in (b).

the inventory and the VPRM data to the grid of each flux footprint using a nearest-neighbor approach. Then, for each grid cell, for each time step, and for each emission sector, we multiplied the re-gridded inventory/VPRM data (µmol m^{-2} s^{-1}) by the respective flux footprint (m^{-2}) and the cell area (m^2), and summed over the entire 15 × 15 km^2 area for which the flux footprints were modeled (in the following denoted as "footprint domain"). To account for flux contributions outside the footprint domain, or for areas without emission data (i.e., outside the administrative boundary of the city of Munich, see Fig. 2), we assumed that the average emissions outside of the footprint domain were equal to the average emissions inside the footprint domain (Christen et al., 2011; Molinier et al., 2026). Since the proportion of the measured flux that originates from within the footprint domain is given by the spatial sum of the flux footprint (i.e., the sum of all footprint function values multiplied by the cell area, dimensionless), we divided the estimated flux (µmol m^{-2} s^{-1}) by this value. In the case of the emission inventory, we only considered the area of the footprint domain in the spatial sum that is within the city boundary. For the quality-controlled data, on average, 93 ± 3 % of the modeled flux originated from within the footprint domain. Modeled $nfCO_2$ fluxes denote the sum of footprint-averaged human respiration fluxes and biofuel emissions from stationary combustion and road transport, as derived from the emission inventory, as well as footprint-averaged NEE derived from the VPRM model. The relative contributions of the individual source sectors to the modeled $ffCO_2$, $nfCO_2$, CO, and NO_x fluxes are provided in Appendix E.

3. Results

3.1. Flux ratios during REA sampling periods

3.1.1. F_{CO}/F_{ffCO_2} ratios

The observation-based F_{CO} and ^{14}C-based F_{ffCO_2} during the 76 REA sampling periods were only weakly correlated ($r = 0.38$, Fig. 5a, Table 1). Except for a few observations with unreasonable negative ratios caused by slightly negative $ffCO_2$ fluxes (within the uncertainties), R_{CO} varied between 1.4 and 17.8 mmol mol^{-1}. The ratios mostly were within the average flux ratios obtained from the emission inventory for the individual source sectors (Fig. 5a, Table 1). The average observation-based flux ratio $\langle R_{CO}\rangle$ was 4.49 ± 0.31 mmol mol^{-1}. With $\langle R_{CO}\rangle$ = 4.49 mmol mol^{-1}, the RMSD between CO-based and ^{14}C-based F_{ffCO_2} of the REA measurements was 9.79 µmol m^{-2} s^{-1} (Table 3). While the ratios did not clearly depend on wind direction or the hour of the day, they were generally lower at low temperatures and higher at high temperatures. Describing $\langle R_{CO}\rangle$ as a linear function of T_{24h} (Appendix C) reduced the RMSD of F_{ffCO_2} to 9.37 µmol m^{-2} s^{-1} (Table 3). 71 % of the RMSD could be attributed to measurement uncertainties, the remaining 29 % (21 % of the average observation-based $ffCO_2$ flux) must have been due to unaccounted variability of R_{CO} (Appendix D).

Table 1
Average observation-based and modeled F_{CO}/F_{ffCO_2} ratios. N is the number of data points considered in the individual subgroups. r describes the Pearson correlation coefficient between F_{CO} and F_{ffCO_2}. $\langle R_{CO}\rangle$ equals the slope of an ODR forced through the origin. In addition, the uncertainty of the slope from the ODR is given.

Data	N [–]	r [–]	$\langle R_{CO}\rangle$ [mmol mol^{-1}]
Observation-based data			
All REA periods	76	0.38	4.49 ± 0.31
For T_{24h}: −4 °C–15 °C	18	0.41	3.31 ± 0.32
5 °C–10 °C	14	0.34	4.04 ± 0.36
10 °C–15 °C	17	0.16	4.36 ± 0.79
15 °C–20 °C	11	0.27	5.27 ± 1.77
20 °C–27 °C	16	0.44	6.74 ± 1.0
Modeled data			
All 30 min periods	3017	0.31	4.48 ± 0.04
07:00–20:00 LT	2140	0.08	4.77 ± 0.05
20:00–07:00 LT	877	0.49	3.31 ± 0.05
REA periods	76	0.4	5.57 ± 0.24
Public power	2140	0.97	0.0507 ± 0.0003
Stationary combustion	2140	0.83	0.98 ± 0.01
Road transport	2140	0.90	8.90 ± 0.03
Off-road transport	2140	0.86	72.92 ± 0.16

The inventory-based R_{CO} values at the REA sampling periods ranged from 3.0 to 11.5 mmol mol^{-1} (Fig. 5b). Considering all 30 min data between 07:00 and 20:00 LT on working days, individual 30 min periods had modeled R_{CO} values as low as 0.5 mmol mol^{-1} due to public power emissions. R_{CO} was often larger than the ratio from road transport due to a substantial F_{CO} contribution from off-road transport (27 % during the day, 49 % at night, see Table E.6). Due to these off-road emissions, F_{CO} was always >0.06 µmol m^{-2} s^{-1} during the day and >0.02 µmol m^{-2} s^{-1} at night. The correlation coefficient r between the modeled F_{CO} and F_{ffCO_2} of all 30 min periods between 07:00 and 20:00

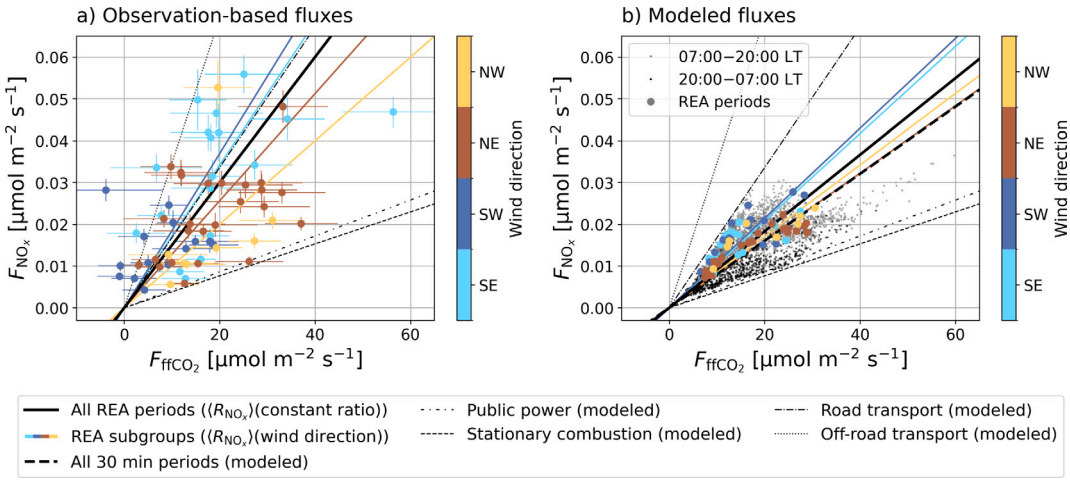


Fig. 6. (a) Observation-based F_{NO_x} and ^{14}C-based F_{ffCO_2} during the REA sampling periods. The colors indicate the mean horizontal wind direction sector. Solid lines illustrate the orthogonal distance regressions (ODR) for all data points and the respective wind direction-based subgroups. For reference, the slopes of the dashed lines represent the average flux ratios of the dominant source sectors obtained from the footprint-averaged emission inventory. (b) Modeled F_{NO_x} and F_{ffCO_2} at the measurement site for all 30 min timestamps of the EC measurements between 07:00 and 20:00 LT (gray) and between 20:00 and 07:00 LT (black), as well as for the 60 min REA sampling periods (colored circles). For clarity, individual data points with modeled F_{ffCO_2} up to 140 µmol m^{-2} s^{-1} were omitted in (b).

LT was 0.08, with an average flux ratio of 4.77 ± 0.05 mmol mol^{-1} (Table 1). At night, the correlation coefficient was higher (r = 0.49), while ⟨R_{CO}⟩ was lower (3.31 ± 0.05 mmol mol^{-1}). For the REA sampling periods, the average modeled flux ratio was ⟨R_{CO}⟩ = 5.57 ± 0.24 mmol mol^{-1}. If F_{ffCO_2} was calculated as $F_{CO}/\langle R_{CO}\rangle$, as with the observation-based fluxes, the NRMSD of the inventory-based fluxes at the REA sampling periods was 41 % (Table 3). As with the observation-based fluxes, the modeled F_{CO}/F_{ffCO_2} ratios tended to increase with temperature due to the smaller relative flux contribution of stationary combustion (which has a much lower ⟨R_{CO}⟩ than road transport) at higher temperatures. Note that the modeled R_{CO} values depended strongly on the emission ratios of road transport considered in the emission inventory. Using the previous version of emission factors (HBEFA 4.2), the modeled ⟨R_{CO}⟩ of all 30 min periods was 28 % lower than with the latest HBEFA 5.1 version presented in Fig. 5 (Appendix F).

3.1.2. F_{NO_x}/F_{ffCO_2} ratios

The observation-based R_{NO_x} values > 0 varied between 0.43 and 7.1 mmol mol^{-1}, with an average ratio of ⟨R_{NO_x}⟩ = 1.5 ± 0.11 mmol mol^{-1} (Fig. 6a, Table 2). With this average ratio, the RMSD between the ^{14}C-based F_{ffCO_2} and the NO_x-based F_{ffCO_2} was 9.77 µmol m^{-2} s^{-1} (Table 3). Measurement uncertainties accounted for 69 % of the RMSD; the remaining 31 % (18 % of the average $ffCO_2$ flux) was due to an unaccounted variability in R_{NO_x} (Appendix D). The correlation coefficient between F_{NO_x} and F_{ffCO_2} was 0.5. On average, R_{NO_x} was 56 % larger for measurements during southerly winds than for measurements during northerly winds (Fig. 6a, Table 2). Considering wind sector-specific ⟨R_{NO_x}⟩ values (Appendix C), slightly reduced the RMSD to 9.66 µmol m^{-2} s^{-1} (Table 2). Unlike for R_{CO}, an ODR through the observation-based F_{NO_x} and F_{ffCO_2} did not reveal a linear dependence on T_{24h}.

The modeled R_{NO_x} values were between the ratios of stationary combustion and road transport in the emission inventory (Fig. 6b). As with CO, off-road transport had a higher ⟨R_{NO_x}⟩ than road transport. However, the difference in the ratios of road transport and off-road transport was smaller than for CO, and off-road emissions contributed only 8 % during the day (14 % at night) to the total modeled NO_x fluxes (Table E.6). The correlation coefficient of all 30 min time periods between 07:00 and 20:00 LT was 0.72, with an average ratio ⟨R_{NO_x}⟩ = 0.85 ± 0.01 mmol mol^{-1}. Similar results were obtained when nighttime data was included (r = 0.71, ⟨R_{NO_x}⟩ = 0.803 ± 0.005 mmol mol^{-1}), though the correlation was slightly higher at night (r = 0.81) and ⟨R_{NO_x}⟩ was lower (0.61 ± 0.01 mmol mol^{-1}). While the minimum modeled flux ratio was only 7 % lower than the minimum observation-based flux ratio > 0, the modeled maximum was 77 % lower (1.7 mmol mol^{-1}). For the REA sampling periods, the modeled ⟨R_{NO_x}⟩ was 0.92 ± 0.03 mmol mol^{-1}. The NRMSD between the modeled F_{ffCO_2} and the modeled $F_{NO_x}/\langle R_{NO_x}\rangle$ at the REA sampling periods was 28 % (Table 3). As with the observations, R_{NO_x} was higher for southerly winds than for northerly winds. Unlike the observation-based flux ratios, the modeled R_{NO_x} generally increased with increasing mean air temperature. With the HBEFA 5.1 emission ratios, the modeled ⟨R_{NO_x}⟩ from all 30 min periods was 8 % higher than with the HBEFA 4.2 ratios (Appendix F).

Table 2
Average observation-based and modeled F_{NO_x}/F_{ffCO_2} ratios. N is the number of data points considered in the individual subgroups. r describes the Pearson correlation coefficient between F_{NO_x} and F_{ffCO_2}. ⟨R_{NO_x}⟩ equals the slope of an ODR forced through the origin. In addition, the uncertainty of the slope from the ODR is given.

Data	N [–]	r [–]	⟨R_{NO_x}⟩ [mmol mol^{-1}]
Observation-based data			
All REA periods	65	0.50	1.50 ± 0.11
For wind from: NE	25	0.46	1.28 ± 0.14
SE	18	0.52	1.71 ± 0.22
SW	14	0.11	1.85 ± 0.34
NW	8	0.36	1.00 ± 0.24
Modeled data			
All 30 min periods	3017	0.71	0.803 ± 0.005
07:00–20:00 LT	2140	0.72	0.85 ± 0.01
20:00–07:00 LT	877	0.81	0.61 ± 0.01
REA periods	65	0.78	0.92 ± 0.03
Public power	2140	0.99	0.43 ± 0.0013
Stationary combustion	2140	0.99	0.3827 ± 0.0006
Road transport	2140	0.99	1.6797 ± 0.0018
Off-road	2140	0.92	3.4663 ± 0.0075

3.2. Half-hourly F_{ffCO_2} and F_{nfCO_2}

3.2.1. Average diurnal cycles per month

Applying ⟨R_{proxy}⟩ (Table 3) to the quality-controlled continuous EC fluxes, the proxy-based $ffCO_2$ fluxes showed distinct diurnal and

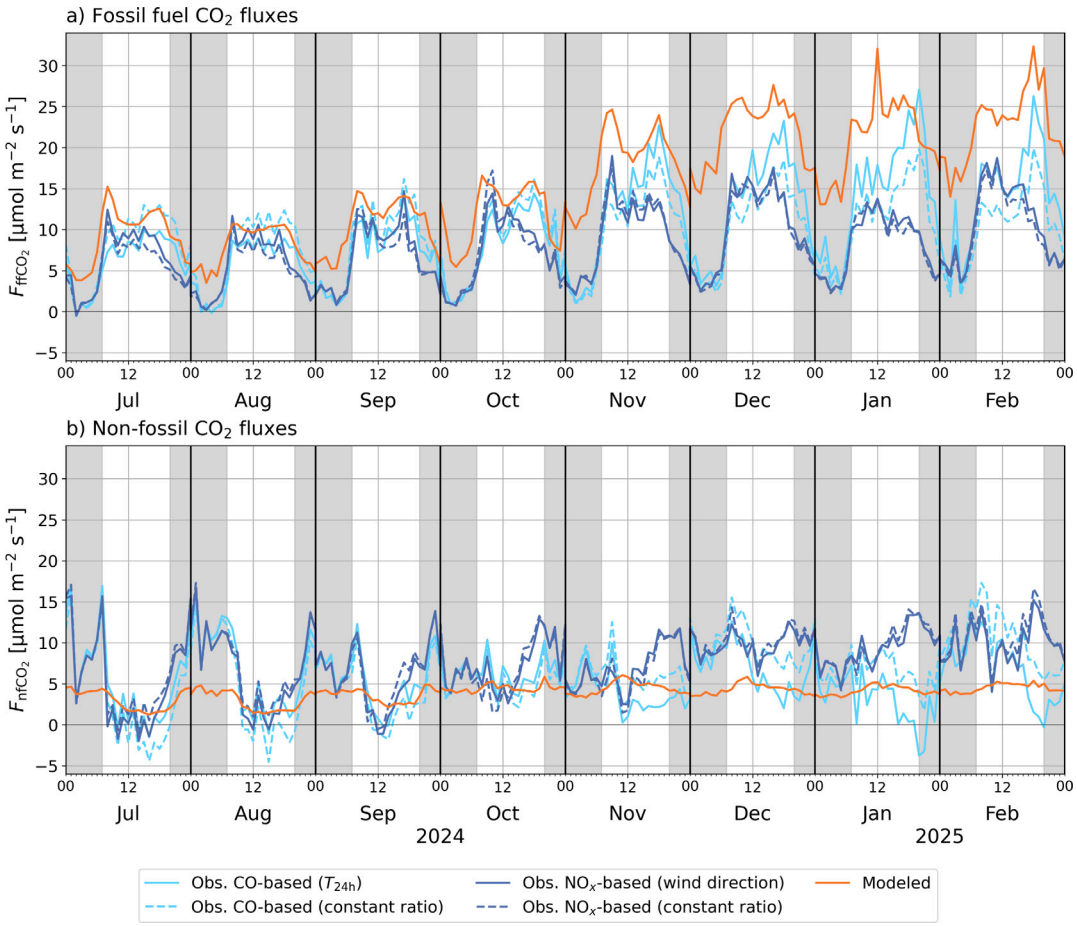


Fig. 7. Monthly averaged F_{ffCO_2} (a) and F_{nfCO_2} (b) for each hour of the day. The timestamps are given in LT and represent the end of the averaging period. The dashed lines depict the observation-based fluxes calculated using a constant $\langle R_{proxy} \rangle$ value. The blue solid lines represent the fluxes calculated with temperature-dependent $\langle R_{CO} \rangle$ and wind direction-dependent $\langle R_{NO_x} \rangle$ values, respectively. The orange line shows the average footprint-weighted inventory and VPRM fluxes.

Table 3
Average F_{proxy}/F_{ffCO_2} ratios $\langle R_{proxy} \rangle$ and root-mean-square deviations (RMSD) between ^{14}C- and proxy-based F_{ffCO_2} using $\langle R_{proxy} \rangle$. $\langle R_{CO} \rangle(T_{24h})$ was obtained by a linear fit through the $\langle R_{CO} \rangle$ values of the five T_{24h}-dependent subgroups of REA measurements (Appendix C). NRMSD denotes the normalized RMSD with respect to the average F_{ffCO_2} due to measurement uncertainties (δ) or an unaccounted variability in the F_{proxy}/F_{ffCO_2} ratio (R). For comparison, the results from the footprint-averaged emission inventory for the REA sampling periods are shown.

Proxy	$\langle R_{proxy} \rangle$ [mmol mol^{-1}]	RMSD [µmol m^{-2} s^{-1}]	NRMSD (δ) [–]	NRMSD (R) [–]
Observation-based data				
CO (const. ratio)	4.49 ± 0.31	9.79	43 %	21 %
CO (T_{24h})	$(0.14 \cdot T_{24h}) + 3.15$	9.37	43 %	18 %
NO_x (const. ratio)	1.5 ± 0.11	9.77	42 %	18 %
NO_x (wind dir)	1.28 ± 0.14 (NE)	9.66	42 %	18 %
	1.71 ± 0.22 (SE)			
	1.85 ± 0.34 (SW)			
	1.00 ± 0.24 (NW)			
Modeled data				
CO (const. ratio)	5.57 ± 0.24	6.64	–	41 %
NO_x (const. ratio)	0.92 ± 0.03	4.59	–	28 %

seasonal patterns (Fig. 7a). In general, the fluxes were larger during the day than at night and larger in the cold season than in the warm season. Between 07:00 and 20:00 LT, the average observation-based F_{ffCO_2} was about 9 µmol m^{-2} s^{-1} for July to September and about 16 µmol m^{-2} s^{-1} for December to February (average of F_{ffCO_2} calculated with $\langle R_{CO} \rangle(T_{24h})$ and $\langle R_{NO_x} \rangle$(wind dir)). There was no significant difference in the NO_x-based fluxes between the approach with a constant $\langle R_{NO_x} \rangle$ and the approach with wind direction-dependent ratios, as all wind directions were considered. For the CO-based approach, the temperature-dependent ratios lead to slightly smaller F_{ffCO_2} in the warm season and slightly larger F_{ffCO_2} in the cold season compared to the constant $\langle R_{CO} \rangle$. In general, CO- and NO_x-based fluxes agreed well. However, from October to February, the CO-based fluxes were considerably larger in the afternoon than the NO_x-based fluxes. While the CO-based fluxes mostly peaked in the morning and in the afternoon, the NO_x-based fluxes were largest around 08:00/09:00 LT and decreased during the day. By definition, the diurnal cycles of the proxy-based $ffCO_2$ fluxes reflected the temporal changes of the COor NO_x fluxes, respectively.

The modeled $ffCO_2$ fluxes were generally larger than the observation-based fluxes. Between 07:00 and 20:00 LT, the modeled fluxes were on average 2.6 µmol m^{-2} s^{-1} larger between July and September and 9.2 µmol m^{-2} s^{-1} larger between December and February. Thus, the modeled seasonal difference was approximately twice as high as the average observed seasonal difference. From July to November, particularly in November, the modeled F_{ffCO_2} showed a characteristic, traffic-dominated pattern with two peaks during the morning and the afternoon rush hours. For the other months, the diurnal pattern was less distinct. At night, the modeled F_{ffCO_2} was

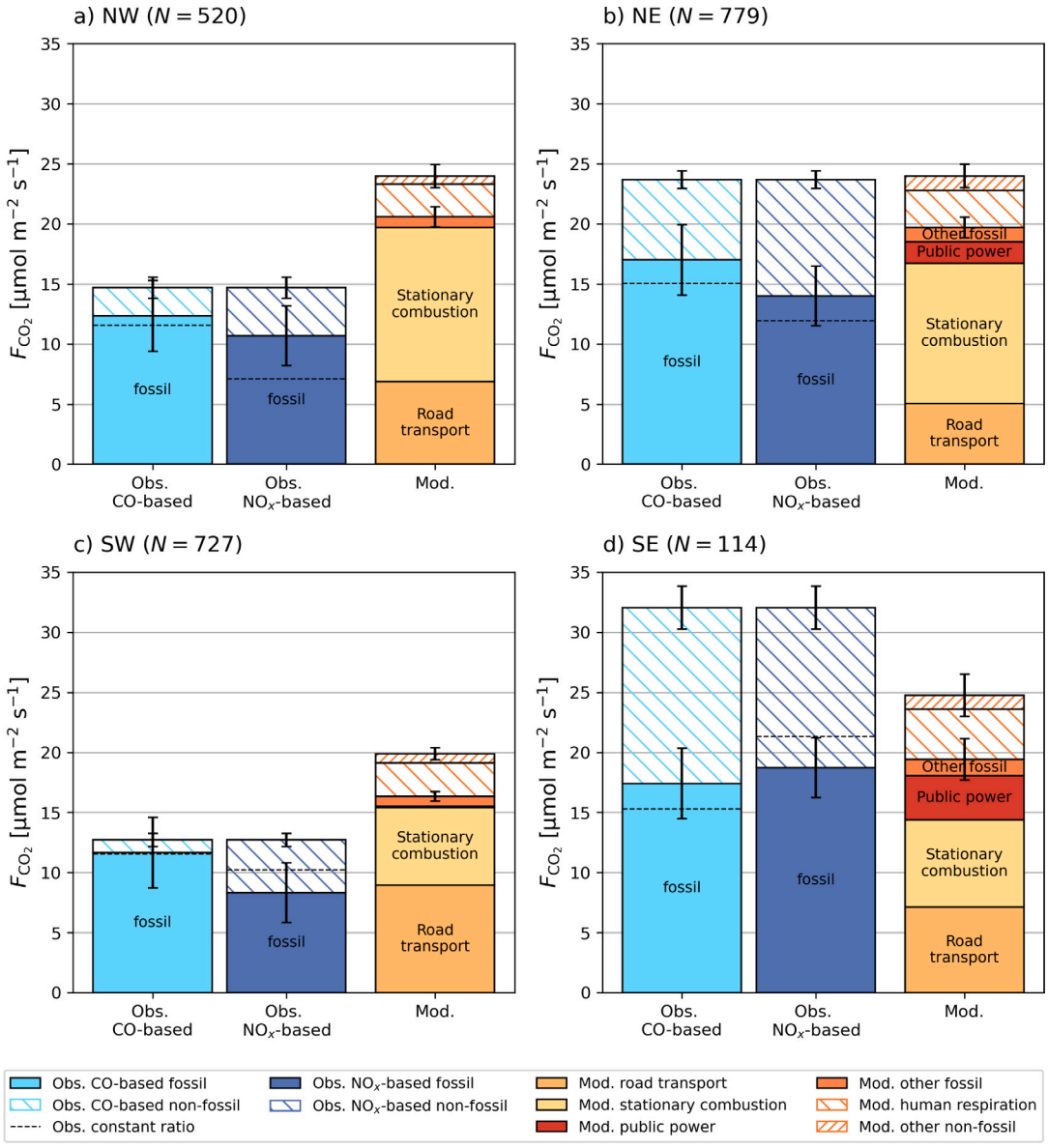


Fig. 8. Average F_{ffCO_2} and F_{nfCO_2} between 07:00 and 20:00 LT on working days for the four cardinal wind directions. To avoid overrepresentation of time periods with more available data (Fig. 3), the fluxes were first averaged per hour, then averaged over all hours. The error bars of the observation-based net F_{CO_2} and of the modeled fluxes represent the uncertainties of the average fluxes (std/$\sqrt{N}$). The error bar of the partitioning of observation-based F_{ffCO_2} and F_{nfCO_2} is about 0.2 times the absolute average F_{ffCO_2}, estimated from a synthetic data experiment (Appendix D). N denotes the number of measurements.

more than twice as high as the observation-based flux, with the largest difference in December.

Both observation-based and modeled $nfCO_2$ fluxes showed clear diurnal cycles in July, August, and September, with lower values during the day and higher values at night (Fig. 7b). However, the amplitude of the diurnal cycles of F_{nfCO_2} were larger for the observation-based than for the modeled fluxes. While the modeled fluxes were always positive, the observation-based fluxes were approximately zero, or slightly negative at noon. From October to February, the modeled fluxes were relatively constant, both on a diurnal and seasonal scale. The observation-based fluxes showed a larger variability, but no distinct diurnal cycles. In January and February, evening fluxes were much higher in the NO_x-based approach than in the CO-based approach, where F_{nfCO_2} was even negative, due to the relatively small NO_x and relatively large CO fluxes. On average, observation-based F_{nfCO_2} between 07:00 and 20:00 LT increased from approximately 1 µmol m^{-2} s^{-1} in July to 8 µmol m^{-2} s^{-1} in January, while the modeled fluxes increased from approximately 2 µmol m^{-2} s^{-1} to 5 µmol m^{-2} s^{-1}.

3.2.2. *Average daytime fluxes per wind sector*

Considering the average wind directions during the flux measurements revealed differences in the fluxes from the east and west (Fig. 8). Net observation-based CO_2 fluxes from the east were approximately twice as high as those from the west. As the $ffCO_2$ fluxes were only slightly larger during easterly than during westerly winds, this difference was mainly due to significantly larger $nfCO_2$ fluxes in the east than in the west. Due to the lower R_{NO_x} values in the south than in the north, the wind direction-dependent $\langle R_{NO_x} \rangle$ lead to slightly lower F_{ffCO_2} in the south and slightly higher F_{ffCO_2} in the north than the approach using a constant ratio independent of wind direction. Except for the southwest, the NO_x-based fluxes agreed better with the CO-based flux estimates when considering spatial variability in R_{NO_x}. Overall, the average CO- and NO_x-based $ffCO_2$ and $nfCO_2$ fluxes agreed within their uncertainties.

The modeled F_{CO_2} did not show such pronounced spatial differences and best agreed with the observation-based fluxes from the

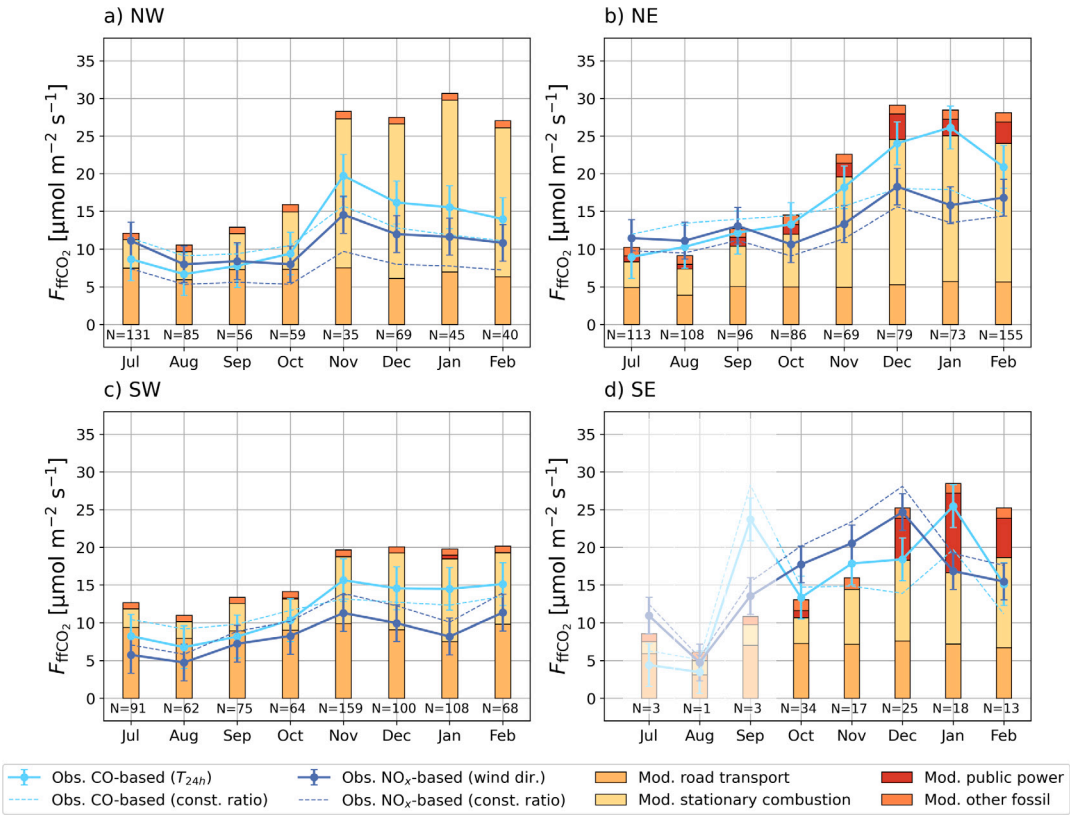


Fig. 9. Monthly averages of F_{ffCO_2} between 07:00 and 20:00 LT for the four cardinal wind directions. To avoid overrepresentation of time periods with more available data (Fig. 3b), the fluxes were first averaged per hour, then averaged over all hours. The error bars are about 0.2 times the absolute average F_{ffCO_2}, estimated from a synthetic data experiment (Appendix D). N denotes the number of measurements. Data with $N < 10$ is shown in faded colors.

northeast. While the magnitude of the modeled F_{ffCO_2} was similar in all four sectors, ranging from 16.3 µmol m^{-2} s^{-1} in the southwest to 20.6 µmol m^{-2} s^{-1} in the northwest, the compositions differed. In the north, stationary combustion contributed the most, in the southwest road transport dominated, and in the southeast, public power had a significant contribution. There were more observations from the northeast (36 %) and the southwest (34 %) than from the northwest (24 %) and from the southeast (5 %). However, the timestamps of the observation-based and modeled data were the same.

Combining spatial, temporal, and sectoral information Fig. 9 shows that the discrepancy between the observation-based and modeled F_{ffCO_2} was largest in the northwest from November to February. The modeled emissions from road transport in the flux footprint were approximately constant throughout the year, with the highest emissions in the footprint for the southwestern sector. In the northeast, emissions from the public power sector were only slightly higher in the cold months than in the warm months. In contrast, substantial public power emissions in the southeast only occurred in December, January, and February. CO- and NO_x-based F_{ffCO_2} mostly agreed within their uncertainties from July to October. Only in the southeast significant differences were observed. From November to February, CO-based fluxes were larger than NO_x-based fluxes in all wind directions, except in the southeast, where NO_x-based fluxes were mostly larger.

3.2.3. Average $nfCO_2$ fluxes in dependence of air temperature and radiation

While the modeled F_{nfCO_2} was similar in magnitude in all wind directions, the observation-based F_{nfCO_2} was much larger in the east than in the west. In all wind directions except for the southeast, F_{nfCO_2} decreased as downwelling shortwave radiation increased (Fig. 10). The decrease was strongest in the northwest, where the average F_{nfCO_2} decreased approximately linearly with shortwave radiation up to about 500 W m^{-2}. For higher shortwave radiation, F_{nfCO_2} did not decrease further and was approximately −3 µmol m^{-2} s^{-1}. In the southeast, F_{nfCO_2} was approximately constant, independent of the downwelling shortwave radiation, which was ≤600 W m^{-2}. The modeled $nfCO_2$ fluxes generally decreased with increasing radiation, but the differences were much smaller. The modeled F_{nfCO_2} was always positive as it was dominated by human respiration.

Similarly, the average F_{nfCO_2} from the west decreased with increasing air temperature when the downwelling shortwave radiation was ≥100 W m^{-2}, i.e., during daylight (Fig. 11). However, at night and in cloudy conditions with downwelling shortwave radiation <100 W m^{-2}, F_{nfCO_2} generally increased with increasing temperature. The relation was less clear for fluxes from the east (Appendix G).

3.2.4. Average fluxes of all timestamps

Between 07:00 and 20:00 LT on working days between 01 July 2024 and 28 February 2025, the average observation-based F_{CO_2} was 17.8 ± 0.6 µmol m^{-2} s^{-1} (Fig. 12a). With $\langle R_{CO}\rangle(T_{24h})$, the CO-based F_{ffCO_2} accounted for approximately 77 % of F_{CO_2}, or 14 ± 3 µmol m^{-2} s^{-1}. NO_x-based separation using $\langle R_{NO_x}\rangle$(wind dir) resulted in a smaller $ffCO_2$ contribution (63 % or 11.3 ± 2.2 µmol m^{-2} s^{-1}, respectively). Similar results were obtained when using constant $\langle R_{proxy}\rangle$. The average CO-based F_{nfCO_2} was 4 ± 3 µmol m^{-2} s^{-1} and the average NO_x-based F_{nfCO_2} was 6.5 ± 2.3 µmol m^{-2} s^{-1}. Particularly the CO-based F_{nfCO_2} agreed well with the average inventory- and VPRM-based F_{nfCO_2} of 3.88 ± 0.13 µmol m^{-2} s^{-1}. The latter was composed of NEE, which was slightly negative, human respiration, which accounted for 76 % of the modeled F_{nfCO_2}, and other anthropogenic $nfCO_2$ emissions from stationary combustion (e.g., wood burning) and road transport (i.e., biofuels) (Appendix E). The inventory-based average F_{ffCO_2} was 46 % larger than the average observation-based estimate

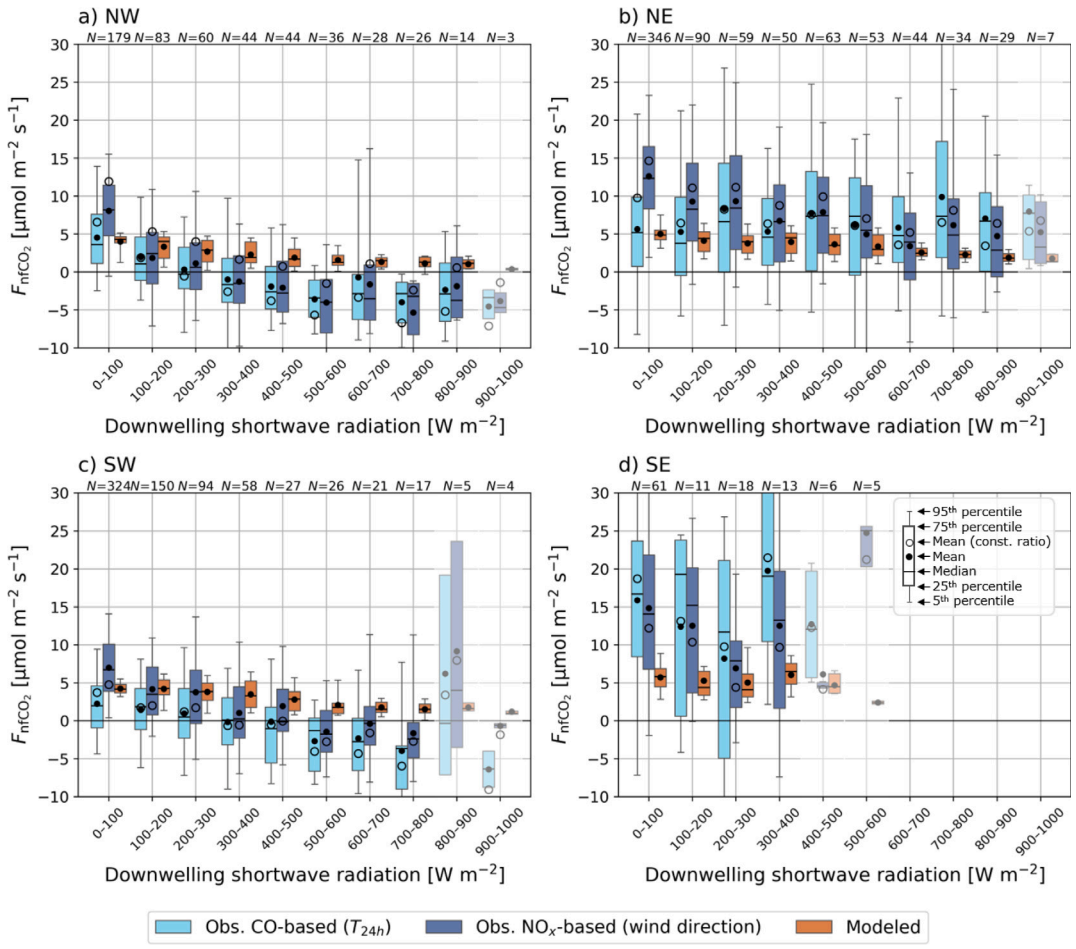


Fig. 10. F_{nfCO_2} between 07:00 and 20:00 LT in dependence on downwelling shortwave radiation for each wind sector. N denotes the number of measurements. Data with $N < 10$ is shown in faded colors.

(18.2 ± 0.6 µmol m^{-2} s^{-1}). It accounted for 82 % of the modeled F_{CO_2}. The largest contributions came from stationary combustion (51 %) and road transport (39 %) (Appendix E).

Including nocturnal data, the average fluxes were generally smaller (Fig. 12b). Due to the small observation-based F_{ffCO_2} at night, the $ffCO_2$ contribution to net observation-based F_{CO_2} was significantly smaller (58 % of F_{CO_2}) when considering all time periods than when considering only daytime fluxes. On the contrary, the relative $ffCO_2$ and $nfCO_2$ contributions in the modeled CO_2 fluxes did not change significantly (80 % fossil).

4. Discussion

4.1. F_{proxy}/F_{ffCO_2} ratios

How well are observation-based and modeled F_{CO} and F_{NO_x} correlated with F_{ffCO_2}, and how do the F_{proxy}/F_{ffCO_2} ratios vary?

The correlation coefficient between the observation-based F_{proxy} and ^{14}C-based F_{ffCO_2} (Tables 1, 2, and 3) were smaller than those reported in other urban studies considering proxy and $ffCO_2$ excess concentrations (e.g., Maier et al., 2024a; Juchem et al., 2025). This can be attributed partly to the generally small signal-to-noise ratio of the ^{14}C-based $ffCO_2$ fluxes and the small number of REA measurements. Generally, a higher correlation was expected between F_{proxy} and F_{ffCO_2} than between F_{proxy} and F_{CO_2}. For the continuous EC fluxes, r was 0.6 for F_{CO} and F_{CO_2}, and 0.7 for F_{NO_x} and F_{CO_2}. However, convolution of the emission inventory with the flux footprints indicated that substantial variability in R_{proxy} and low correlations between F_{proxy} and F_{ffCO_2} could still be real effects. Due to variability in the emission ratios between and within the different emission sectors within the flux footprint, the variability in flux ratios at the urban tall tower is likely larger than the variability in ratios of aggregated excess concentrations (compare modeled and observed variability in Rosendahl (2022) and Maier et al. (2024a), for example). The observation-based and modeled correlations were worse for F_{CO} than for F_{NO_x}. This could be explained by the highly variable R_{CO} values of the different emission sectors. Based on the emission inventory, R_{CO} ranged from 0.05 mmol mol^{-1} for public power to 72.9 mmol mol^{-1} for off-road transport (Table 1). In addition, stationary combustion ratios varied due to different fuel types for heating (oil, gas, and wood). In contrast, R_{NO_x} only varied by a factor of four in the inventory-based F_{ffCO_2} estimates (Fig. 6, Table 2). A better correlation between $ffCO_2$ and NO_x than between $ffCO_2$ and CO has also been reported by Rosendahl (2022).

The air temperature dependence of the observation-based R_{CO} was consistent with the expectation of more stationary combustion in the cold (heating) than in the warm season (non-heating). Accordingly, air temperature dependence in R_{NO_x}, and other dependencies, e.g., on the hour of the day, would also have been expected. Due to the better data coverage during the day than at night, modeled $\langle R_{proxy} \rangle$ considering only data between 07:00 and 20:00 LT was similar to $\langle R_{proxy} \rangle$ of all quality-controlled modeled fluxes. However, the modeled R_{CO} was 44 % larger during the day than at night, and R_{NO_x} was 39 % larger (Tables 1 and 2). Resolving diurnal cycles in R_{proxy} was restricted by the small signal-to-noise ratio, the small number of measurements, and the multitude of parameters that determine the flux ratios. Not accounting for variability in R_{proxy} increases the uncertainty and potential bias in F_{ffCO_2} (Section 4.2).

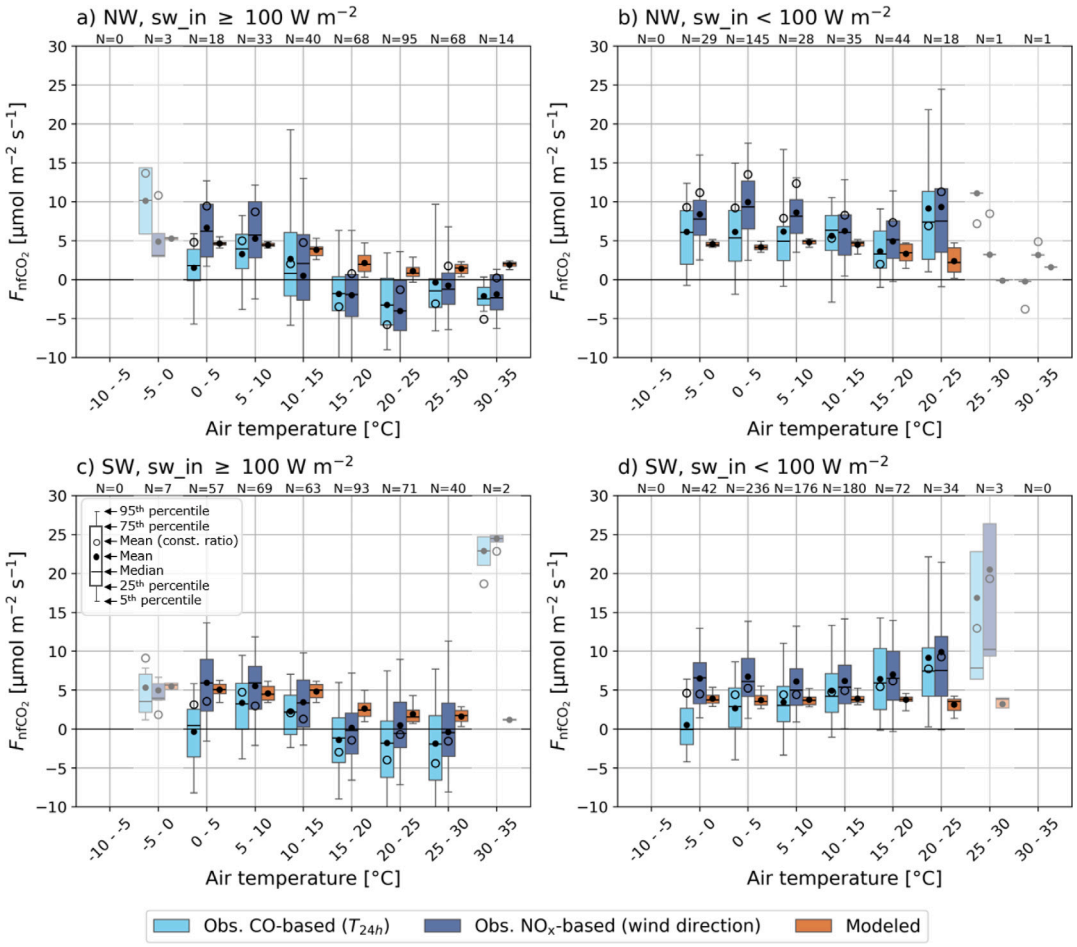


Fig. 11. F_{nfCO_2} in dependence on air temperature during the 30 min averaging intervals. (a) and (c) include timestamps when the downwelling shortwave radiation (sw_in) was ≥100 W m^{-2}, while (b) and (d) include timestamps when sw_in was <100 W m^{-2} for the northwest and southwest wind sectors, respectively. The sw_in <100 W m^{-2} category includes nighttime data. Data with $N < 10$ is shown in faded colors. Corresponding figures for the northeast and the southeast are presented in Appendix G.

How do observation-based and modeled average F_{proxy}/F_{ffCO_2} ratios compare?

For CO, the modeled $\langle R_{CO} \rangle$ from the REA periods was 24 % higher than the observation-based $\langle R_{CO} \rangle$. The overestimation of R_{CO} indicates that the contribution from road transport was overestimated in the emission inventory or in the footprint modeling, or that the modeled $\langle R_{CO} \rangle$ for road transport was too high. In addition, the contribution from off-road transport could have been overestimated in the emission inventory. Off-road emissions only contributed 2.1 % to the modeled F_{ffCO_2}, but due to their very high F_{CO}/F_{ffCO_2} ratio, they accounted for 27 % of the modeled F_{CO} (Table E.6). Modeled off-road emissions were highly uncertain due to limited knowledge of their spatial and temporal variability at neighborhood scale. Off-road emissions were downscaled based on different land use types defined in the CORINE Land Cover 2018 and the ESA WorldCover 2021. Although several studies have shown that off-road emissions from railways and mobile machinery exhibit diurnal, weekly, and seasonal variability (Super et al., 2023), and that the emission factors depend strongly on the engine speed and load and operating conditions (e.g., Abolhasani et al., 2008; Zavala et al., 2017), off-road emissions were assumed to be constant over time as no temporal profiles were available for this sector (Dröge et al., 2024). An overestimation of the CO emissions from off-road transport is further supported by the fact that the NRMSD between the ^{14}C-based F_{ffCO_2} and the CO-based F_{ffCO_2} attributed to an unaccounted variability in R_{CO} was approximately 20 % smaller than the NRMSD in an analogous inventory-based calculation (Table 3), indicating that the R_{CO} variability was overestimated in the inventory.

For NO_x, the modeled $\langle R_{NO_x} \rangle$ from the REA periods was 39 % lower than the observation-based $\langle R_{NO_x} \rangle$. The observation-based R_{NO_x} was often higher than the modeled R_{NO_x} for road transport, suggesting that the latter was underestimated in the emission inventory. A substantial underestimation of F_{NO_x}/F_{ffCO_2} from the most recent traffic models has also been reported by Karl et al. (2017) for the city of Innsbruck.

4.2. Proxy-based $ffCO_2$ flux estimation

Can observation-based and/or modeled F_{proxy}/F_{ffCO_2} ratios be used to calculate continuous $ffCO_2$ fluxes and how large is their uncertainty?

Based on the REA measurements, measurement uncertainties and neglect of the R_{proxy} variability caused an uncertainty in the half-hourly, proxy-based F_{ffCO_2} values of about 64 % (9.8 μmol m^{-2} s^{-1}) for both the CO- and the NO_x-based approaches (Table 3). Since approximately 70 % of this uncertainty was due to measurement uncertainties, using different ratios for different temperatures or wind directions (Appendix C) reduced the uncertainty by less than 0.5 μmol m^{-2} s^{-1} (Table 3). For individual half-hour periods, the REA-based uncertainty may be underestimated due to the limited number of REA measurements. However, for the quality-controlled EC dataset analyzed in this study, in which time periods with exceptionally large proxy fluxes and with spikes in the proxy concentrations were excluded (Section 2.1.2), an uncertainty of 9.8 μmol m^{-2} s^{-1} for half-hourly F_{ffCO_2} is considered reasonable. Neglecting the variability in R_{proxy} thus increases the uncertainty of the proxy-based F_{ffCO_2} estimates by about 53 % compared to

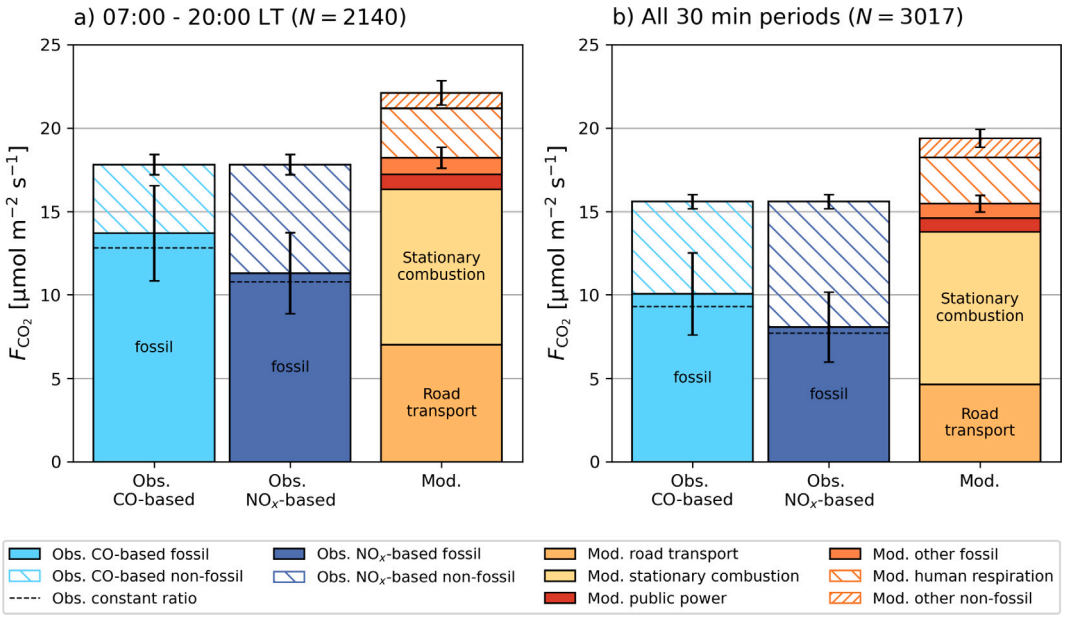


Fig. 12. Average F_{ffCO_2} and F_{nfCO_2} considering data between 07:00 and 20:00 LT (a), and all EC timestamps (b). To avoid overrepresentation of time periods with more available data (Fig. 3b), the fluxes were first averaged per hour, then averaged over all hours. The error bars of the observation-based net F_{CO_2} and of the modeled fluxes represent the uncertainties of the average fluxes (std/$\sqrt{N}$). The error bar of the partitioning of F_{ffCO_2} and F_{nfCO_2} is about 0.2 times the absolute average F_{ffCO_2}, estimated from a synthetic data experiment (Appendix D). N denotes the number of measurements.

direct ^{14}C-based F_{ffCO_2} estimates. However, the statistical uncertainty from neglecting R_{proxy} variability is negligible when averaging a large number of proxy-based F_{ffCO_2} estimates.

While the uncertainty of individual half-hourly, proxy-based F_{ffCO_2} estimates is negligible when calculating average fluxes, a synthetic data experiment that considered measurement uncertainties, unaccounted variability in R_{proxy}, sampling bias due to the limited number of REA measurements, and uncertainties in average values calculated from an ODR forced through the origin suggested that the uncertainty of average, proxy-based daytime F_{ffCO_2} was 23 % or 2.9 µmol m^{-2} s^{-1} for the CO-based approach and 19 % or 2.4 µmol m^{-2} s^{-1} for the NO$_x$-based approach (Appendix D). The modeled bias in average daytime fluxes using a constant $\langle R_{proxy} \rangle$ from the selected REA sampling periods was <5 %, whereas the modeled proxy-based F_{ffCO_2} of individual months or hours of the day had a bias of up to 46 % (Appendix D). There was also a systematic underestimation of nighttime F_{ffCO_2} by about 25 %–35 % due to reduced traffic and consequently lower R_{proxy} at night (Table 1, Table 2, Appendix D). Based on the synthetic data experiment, we assumed an uncertainty of about 20 % in average daytime F_{ffCO_2}, noting that temporally or spatially resolved F_{ffCO_2} can be biased by up to 50 % (Appendix D). These uncertainty estimates rely on the variability of R_{proxy} in the emission inventory, which may be overestimated, particularly for CO (Section 4.1). Moreover, the synthetic data experiments did not consider a parametrization of $\langle R_{proxy} \rangle$ on temperature or wind direction, as was done in the observations. The latter is expected to reduce the bias. The results also depend on the time periods considered in the ODR.

An independent measure of the uncertainty in the proxy-based fluxes was the difference between the CO- and the NO$_x$-based approaches. If $\langle R_{proxy} \rangle$ was representative of the considered measurement periods, both approaches should result in the same F_{ffCO_2} estimate. The overall good agreement between CO- and NO$_x$-based F_{ffCO_2} indicated the efficacy of the flux partitioning approach and the uncertainty estimation. Despite the low correlation and the sparse data coverage, the REA and EC measurements thus suggest that observation-based $\langle R_{proxy} \rangle$ values can be used to calculate purely observation-based average daytime $ffCO_2$ and $nfCO_2$ fluxes with an uncertainty of about 20 %. Based on the observations, CO and NO$_x$ were equally suited for this purpose. Due to differences between observation-based and modeled $\langle R_{proxy} \rangle$ values and not yet quantified uncertainties in the inventory-based fluxes, F_{ffCO_2} should always be calculated using observation-based F_{proxy}/F_{ffCO_2} ratios.

4.3. Continuous $ffCO_2$ and $nfCO_2$ flux estimates

How large are the contributions from fossil and non-fossil emissions to net CO_2 fluxes and how do observation-based and modeled fluxes compare?

From 01 July 2024 to 28 February 2025, the average observation-based F_{ffCO_2} from the 30 min timestamps between 07:00 and 20:00 LT, with quality-controlled EC and inventory data, was 12.5 µmol m^{-2} s^{-1}. This corresponded to 70 % of the net EC CO_2 flux during these time periods (Fig. 12). Overall, the CO-based and the NO$_x$-based F_{ffCO_2} and F_{nfCO_2} agreed well with each other and with the footprint-averaged emission inventory and VPRM results. While differences between the CO- and the NO$_x$-based flux estimates indicate limited representativeness of the ^{14}C-calibrated ratios from the REA periods, differences between the observation-based and the modeled fluxes can help identify potential improvements or refinements to the emission inventory and the flux footprint modeling, as described below.

Seasonal cycle. The proxy-based $ffCO_2$ flux estimates were on average 78 % larger in the cold season (December – February) than in the warm season (July – September). Due to higher $ffCO_2$ emissions from heating, seasonal differences were expected and were similarly captured in the emission inventory (Figs. 7, 9). However, the amplitude of the seasonal cycle of F_{ffCO_2} was approximately twice as high in the emission inventory as in the observation-based fluxes. Due to the limited resolution of the R_{proxy} variability, the observation-based monthly averages of F_{ffCO_2} could be over- or underestimated by up to 50 % (Section 4.2, Appendix D). This potential bias would further reduce the seasonal difference, indicating that the emission inventory overestimated the amplitude of the seasonal cycle. Assuming that modeled emissions from road transport were approximately constant throughout the year, the increased difference between the modeled and observation-based F_{ffCO_2} in the cold season indicates an overestimation of the stationary combustion component in the emission inventory. This overestimation

was most pronounced in the northwest (Fig. 9). In the northwest, the modeled stationary combustion emissions were much larger than in the south because heating there is primarily based on burning natural gas, whereas in the south, a larger fraction of buildings are supplied by district heating (Aigner et al., 2026).

Public power. Although the stationary combustion fluxes were smaller in the southeast, the modeled total $\mathrm{ffCO_2}$ fluxes were similar to or even larger than for the other wind sectors due to a substantial contribution from public power (power plant south) in winter (Fig. 9). The observation-based $F_{\mathrm{ffCO_2}}$ was also higher in the southeast than in the other wind sectors. However, due to local wind conditions, significantly fewer measurements were taken from the southeast, reducing the representativeness of the results from this wind sector. Furthermore, the modeled fluxes from public power were subject to substantial uncertainty. While the input data are considered to be relatively accurate (Aigner et al., 2026), the contribution of public power emissions to the flux at the measurement site, calculated via FFP, was a major source of uncertainty. The footprint model by Kljun et al. (2015) has been proven suitable for urban environments in several previous studies (e.g., Wu et al., 2022; Fasano et al., 2026; Molinier et al., 2026); however, it does not account for increased emission heights and plume rise from stacks of large power plants. Further analysis of the results from the southeast requires a longer time series of measurements and adjustments to the footprint modeling.

Diurnal cycles. The larger contribution of road transport in the warm season than in the cold season was also apparent in the peaks of observation-based and modeled $F_{\mathrm{ffCO_2}}$ at around 08:00 and 18:00 LT from July to November, and their absence or lower amplitude from December to February (Fig. 7). However, the number of measurements and the wind directions were different for each month. In January evening, the CO-based $F_{\mathrm{ffCO_2}}$ was much larger than the NO_x-based $F_{\mathrm{ffCO_2}}$, due to comparatively large CO and rather small NO_x fluxes. Using the constant or temperature-dependent $\langle R_{\mathrm{CO}} \rangle$, the CO-based $\mathrm{ffCO_2}$ fluxes were larger than the net $\mathrm{CO_2}$ fluxes, resulting in unreasonably large negative $\mathrm{nfCO_2}$ fluxes for a winter evening. This indicates that $\langle R_{\mathrm{CO}} \rangle$ was not representative of an isolated analysis of January afternoons, where the "true" $F_{\mathrm{CO}}/F_{\mathrm{ffCO_2}}$ ratio was probably higher. In general, the NO_x-based fluxes were often lower in the afternoon than the CO-based fluxes, indicating an overestimation of $\langle R_{\mathrm{NO}_x} \rangle$ and/or an underestimation of $\langle R_{\mathrm{CO}} \rangle$ during these time periods. An overestimation of $\langle R_{\mathrm{NO}_x} \rangle$ and/or an underestimation of $\langle R_{\mathrm{CO}} \rangle$ in winter afternoons could, for example, be caused by residential wood burning that was not adequately captured by the REA measurements.

At night, the observation-based $F_{\mathrm{ffCO_2}}$ was on average 59 % lower than the modeled estimate. Consequently, the average $\mathrm{ffCO_2}$ contribution to observation-based day- and nighttime $\mathrm{CO_2}$ fluxes (58 %) was substantially lower than when considering daytime fluxes only (70 %), and lower than in the inventory-based fluxes (80 %) (Fig. 12). Although observation-based $F_{\mathrm{ffCO_2}}$ were likely underestimated at night (Sections 4.1, 4.2), the sampling bias could not explain the significant difference in nocturnal $F_{\mathrm{ffCO_2}}$, indicating that $F_{\mathrm{ffCO_2}}$ was overestimated in the emission inventory at night.

Non-fossil $\mathrm{CO_2}$: Biospheric signals. The decrease in observation-based $F_{\mathrm{nfCO_2}}$ with increasing shortwave radiation and air temperature during the day, particularly in the northeast and southeast (Figs. 10, 11), was a clear biospheric signal. However, the variability, e.g., the amplitude of the diurnal cycles in the warm months, was much smaller for the observation-based $F_{\mathrm{nfCO_2}}$ than for NEE measured in several parks in Munich close to the tall tower (Li et al., 2026). Apparently, biospheric fluxes contributed, on average, only a small fraction to the turbulent flux at the measurement site. Since $F_{\mathrm{nfCO_2}}$ was mostly positive, even during the day in the warm season, human respiration and anthropogenic $\mathrm{nfCO_2}$ emissions must have played a significant role. A minor role of biospheric fluxes and a major role of human respiration was also indicated by the modeled $F_{\mathrm{nfCO_2}}$ (Figs. 7b, 10, and 11; Appendix E). The modeled variability in $F_{\mathrm{nfCO_2}}$ both within and across different temperature regimes and hours of the day was smaller than the observation-based variability. As the VPRM model results showed good agreement with biospheric in situ measurements conducted in three urban parks close to the measurement site (Li et al., 2026), it must be further investigated whether and to which degree the difference in the variability was caused by an underestimation of the biospheric component, by an underestimation of the variability of human respiration, or by the measurement uncertainties that limited the resolution of the relatively small $\mathrm{nfCO_2}$ fluxes. Due to the relatively small fraction of vegetated area within the main flux footprint, i.e., closer to the measurement site (Section 2.1.1), the average biospheric flux contribution of the entire city domain is expected to be much larger than the biospheric flux contribution at the measurement site (Table E.6). For the entire city of Munich, Li et al. (2026) found that biospheric daytime uptake can match or even exceed anthropogenic $\mathrm{ffCO_2}$ emissions in the warm months.

Non-fossil $\mathrm{CO_2}$: Anthropogenic signals. As the fraction of vegetated area east of the tower was only slightly smaller than in the west (Section 2.1.1), the large observation-based $F_{\mathrm{nfCO_2}}$ component in the east, particularly in the southeast, was likely due to human activity. Human respiration fluxes were expected to be higher in the southeast due to the increased number of people at the central railway station and in the city center. The spatial variability in human respiration, however, was already included in the emission inventory and only contributed about 1 $\mu\mathrm{mol\,m^{-2}\,s^{-1}}$. Therefore, the large $\mathrm{nfCO_2}$ emissions were probably caused by non-respiratory human activity. One possible explanation is $\mathrm{nfCO_2}$ emissions resulting from fermentation processes in a brewery. One of the five largest breweries in Munich is located 200 m southeast of the tower, within the peak footprint contribution, and has been identified as a possible source of large $\mathrm{nfCO_2}$ fluxes estimated from the $^{14}\mathrm{C}$ REA measurements (Kunz et al., 2025b). These non-fossil emissions were not included in the emission inventory and could explain a discrepancy between modeled and observation-based $\mathrm{nfCO_2}$ fluxes. Nevertheless, a small, superimposed biospheric signal, i.e., a temperature- and radiation-dependence of $F_{\mathrm{nfCO_2}}$, would have been expected also in the southeast. A temperature- or radiation-dependence of $F_{\mathrm{nfCO_2}}$ in the southeast could not be confirmed by the measurements as there were few or no measurements from the southeast with very high temperatures and large downwelling shortwave radiation (Fig. 10d).

5. Conclusions

Combining continuous tall-tower eddy covariance (EC) CO and NO_x fluxes with discrete, $^{14}\mathrm{C}$-based fossil fuel (ff) $\mathrm{CO_2}$ flux estimates from co-located relaxed eddy accumulation (REA) measurements demonstrated the benefits and challenges of CO- or NO_x-based estimation of $\mathrm{ffCO_2}$ fluxes ($F_{\mathrm{ffCO_2}}$), and the subsequent calculation of non-fossil $\mathrm{CO_2}$ fluxes ($F_{\mathrm{nfCO_2}}$), in urban environments. Based on tall-tower flux measurements conducted near the city center of Munich from July 2024 to February 2025, average daytime $F_{\mathrm{ffCO_2}}$ and $F_{\mathrm{nfCO_2}}$ can be estimated from EC CO or NO_x fluxes assuming a constant, representative, observation-based $F_{\mathrm{proxy}}/F_{\mathrm{ffCO_2}}$ ($\langle R_{\mathrm{proxy}} \rangle$) ratio with an uncertainty of about 20 %. Individual half-hourly $F_{\mathrm{ffCO_2}}$ estimates can have uncertainties of about 60 % due to the limited ability to accurately determine the temporally varying R_{proxy}. Unrepresentative ratios can be identified by differences between CO- and NO_x-based $\mathrm{ffCO_2}$ flux estimates, highlighting the benefit of a multi-species analysis. When analyzing spatial or temporal patterns, such as diurnal or seasonal cycles, the variability of R_{proxy} should be considered. Based on the tall-tower flux measurements, CO and NO_x are both similarly suitable for $F_{\mathrm{ffCO_2}}$ estimation. While EC NO_x measurements require two optical lasers and are generally more challenging than EC CO measurements, a smaller variability in R_{NO_x} than in R_{CO} may better justify the use of one constant

average F_{proxy}/F_{ffCO_2} ratio for NO_x. For CO, seasonal cycles in R_{CO} should be taken into account. Better accounting for the variability in R_{proxy} requires a larger number of REA $^{14}CO_2$ measurements than in the current study ($N = 76$), including measurements at night, and higher signal-to-noise ratios. However, the number of measurements and the signal-to-noise ratio are limited by the strict requirements for successful REA $^{14}CO_2$ measurements, the source strength within the flux footprint, and the current $^{14}CO_2$ measurement precision. Therefore, further investigation of the integration of information from emission inventories, continuous EC F_{proxy}/F_{CO_2} ratios, observation-based F_{proxy}/F_{ffCO_2} ratios of individual source sectors or proxy/$ffCO_2$ ratios of excess concentrations is warranted.

Application of the ^{14}C-calibrated F_{proxy}/F_{ffCO_2} ratios to continuous EC CO and NO_x fluxes measured at the Munich tall tower indicated that the average observation-based F_{ffCO_2} during the daytime on working days accounted for 70 % of the observation-based net CO_2 flux. Although $nfCO_2$ fluxes were more difficult to resolve due to their smaller magnitude, the general dependence of F_{nfCO_2} on air temperature and downwelling shortwave radiation west of the measurement site revealed a biospheric signal in the net CO_2 fluxes at the Munich tall tower. Predominantly positive observation-based F_{nfCO_2} indicated a major contribution from human respiration fluxes. Large observation-based $nfCO_2$ fluxes without clear temperature- or radiation-dependence east of the tower could be related to emissions from a nearby brewery.

The comparison of the observation-based F_{proxy}/F_{ffCO_2} ratios and the observation-based continuous F_{ffCO_2} and F_{nfCO_2} time series with modeling results highlighted the benefits from comparing two completely independent methodological approaches for future methodological improvements. In Munich, the comparison indicated that the F_{NO_x}/F_{ffCO_2} ratio of road transport was likely underestimated in the emission inventory, underscoring the challenges and uncertainties involved in accurately representing the fleet composition and emission factors for different engine types, fuels, and driving patterns. The importance of accurately representing the emission factors from road transport for modeling greenhouse gas emissions was also shown by the significantly lower modeled R_{CO} values in a previous version of the emission inventory that used HBEFA 4.2 emission factors (Appendix F). Substantial off-road contributions to modeled CO emissions limited the comparison of observation-based $\langle R_{CO} \rangle$ with individual source sectors in the emission inventory, as well as the suitability of CO as a proxy for $ffCO_2$ emissions from an inventory perspective. To reduce the uncertainty in modeled off-road emissions, the downscaling of off-road emissions or a bottom-up emission estimation should be investigated further. While the observation-based and modeled continuous F_{ffCO_2} estimates generally agreed well during the day in the warm months, increased differences at night and in the cold months showed that sampling bias in the observation-based approach and stationary combustion fluxes in the emission inventory should be investigated further. To validate large point-source emissions from power plants, the elevated emission height should be considered in the flux footprint modeling. Similarly, the comparison of the observation-based and modeled $nfCO_2$ fluxes showed that both methodological approaches capture diurnal cycles and dependence on air temperature and downwelling shortwave radiation. However, the magnitude of the variability in F_{nfCO_2} requires further investigation. The fact that the observation-based F_{nfCO_2} estimates during south-easterly winds were much larger than the modeled fluxes underscored the necessity of including non-respiratory anthropogenic $nfCO_2$ emission sources, such as breweries and waste-burning facilities, in emission inventories.

Funding

The authors have received funding from ICOS Cities, a.k.a. the Pilot Applications in Urban Landscapes – Towards integrated city observatories for greenhouse gases (PAUL) project, from the European Union's Horizon 2020 research and innovation program under grant agreement no. 101037319. The TUM authors are partly supported by the ERC Consolidator Grant CoSense4Climate (grant no. 101089203). Additional support was provided by internal funds and staff at the Universities of Heidelberg, Freiburg, and the Max Planck Institute for Biogeochemistry in Jena, as well as by the Swedish Strategic Research Area "ModElling the Regional and Global Earth system", MERGE, funded by the Swedish government.

CRediT authorship contribution statement

Ann-Kristin Kunz: Writing – original draft, Visualization, Methodology, Investigation, Formal analysis, Conceptualization. **Samuel Hammer:** Writing – review & editing, Supervision, Project administration, Funding acquisition, Conceptualization. **Patrick Aigner:** Writing – review & editing, Investigation (Inventory). **Lars Borchardt:** Writing – review & editing, Resources. **Jia Chen:** Writing – review & editing, Inventory, VPRM, Resources. **Julian Della Coletta:** Writing – review & editing, Investigation (Flask analysis). **Markus Eritt:** Writing – review & editing, Resources. **Ronny Friedrich:** Writing – review & editing, Investigation (Flask analysis). **Xochilt Gutiérrez:** Writing – review & editing, Investigation (Flask analysis). **Rainer Hilland:** Writing – review & editing, Investigation (EC measurements). **Christopher Holst:** Writing – review & editing, Project administration. **Armin Jordan:** Writing – review & editing, Investigation (Flask analysis). **Natascha Kljun:** Writing – review & editing, Footprints, Supervision, Resources, Funding acquisition. **Richard Kneißl:** Writing – review & editing, Resources. **Daniel Kühbacher:** Writing – review & editing, Investigation (Inventory). **Changxing Lan:** Writing – review & editing, Investigation (EC measurements). **Junwei Li:** Writing – review & editing, Investigation (VPRM). **Betty Molinier:** Writing – review & editing, Investigation (Footprints). **Susanne Preunkert:** Writing – review & editing, Investigation (Flask analysis). **Andreas Christen:** Writing – review & editing, Supervision, Project administration, Funding acquisition, Conceptualization.

Declaration of competing interest

The authors declare that they have no known competing financial interests or personal relationships that could have appeared to influence the work reported in this paper.

Acknowledgments

We thank the following people for their contributions to this work: Virgile Legendre (MPI-BGC, Germany) for his substantial contribution to the construction of the REA flask sampler; Josh Hashemi, Felix Baab, and Dirk Redepenning (University of Freiburg, Germany) for building the hardware at the REA inlet and logistics; Carsten Jahn (KIT, Germany) for negotiations and installations at the Munich measurement site; Christian Becker and Klaus Kürzinger (TUM, Germany) for regular maintenance and logistics related to the REA flask sampler; Steffen Knabe and the entire staff of the ICOS Flask and Calibration Laboratory in Jena and the ICOS Central Radiocarbon Laboratory in Heidelberg for measuring the test and REA flasks; Matthias Zeeman (University of Freiburg, Germany) for managing the data infrastructure; Giacomo Nicolini (CMCC Foundation - Euro-Mediterranean Center on Climate Change) and the entire ICOS ETC staff for processing EC data for the flux footprints. We would also like to thank the three anonymous reviewers for their comments and suggestions, which helped to improve this article. We kindly acknowledge the use of meteorological data provided by the Meteorological Institute of the Ludwig-Maximilian University (LMU). DeepL was used for grammar and spell checking. The Scientific color maps managua and bam (Crameri, 2023) were used to prevent visual distortion of the data and exclusion of readers with color-vision deficiencies (Crameri et al., 2020).

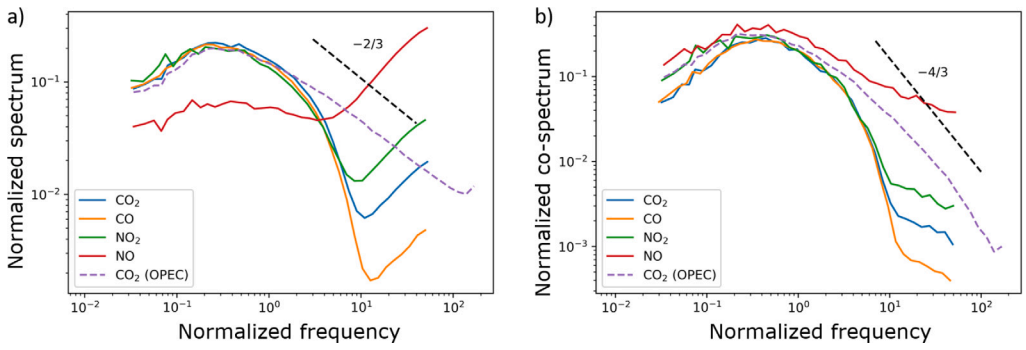


Fig. A.13. Normalized spectra and co-spectra as function of the normalized frequency for CO_2, CO, NO_2, and NO measured by the MGA[7] as well as for CO_2 measured by the open-path IRGASON instrument (OPEC) at the EC tall tower in Munich between July 2024 and February 2025, calculated before the application of spectral corrections. The normalized frequency is given by $n = fz/U$, the normalized spectra by $nS_{\chi'\chi'}/\overline{\chi'\chi'}$, and the normalized co-spectra by $nC_{w'\chi'}/\overline{w'\chi'}$, with f being the frequency, z the measurement height, U the mean horizontal wind speed, χ' the fluctuations of the mole fraction, w' the fluctuations of the vertical wind velocity, $S_{\chi'\chi'}$ the power spectral density of χ', and $C_{w'\chi'}$ the co-spectrum between w' and χ'. Dashed black lines indicate the theoretical slopes according to Kaimal et al. (1972).

Appendix A. Eddy covariance measurements

To calculate net CO_2, CO, and NO_x fluxes, we upsampled the 10 Hz MGA[7] measurements to 20 Hz using a nearest-neighbor approach, and synchronized the MGA[7] measurements with the vertical wind measurements of the IRGASON based on a comparison of the high-frequency time series of CO_2 molar mixing ratios from the MGA[7] and the IRGASON, as described in Hilland et al. (2025b) and Kunz et al. (2026a). We performed coordinate rotation via double rotation (Wilczak et al., 2001) and defined turbulent fluctuations by block averaging (Rebmann et al., 2012) using a 30 min averaging period as suggested in Lan et al. (2024). To account for high-frequency spectral attenuation in the intake line of the MGA[7], indicated by differences between the spectra and co-spectra of the MGA[7] and the open-path IRGASON before the application of spectral corrections at normalized frequencies $>10^0$ (Fig. A.13), we applied the low-pass correction according to Fratini et al. (2012). High-pass filtering effects were corrected according to Moncrieff et al. (2004). While NO measurements contained substantial noise in the high-frequency regime, the average normalized spectra and co-spectra of CO_2 CO, and NO_2 measured by the MGA[7] showed good agreement with standard EC CO_2 measurements by the IRGASON at normalized frequencies $\leq 10^0$, where most turbulent energy is found (Fig. A.13). Good agreement between the IRGASON and theoretical slopes according to Kaimal et al. (1972) throughout the inertial subrange indicates well-measured spectra from the open-path instrument against which spectral corrections can be made. For the flux periods with quality control flags <2, the median spectral correction factor for all MGA[7] species was 1.04 ± 0.02, indicating median spectral losses of 4 %. After spectral corrections and filtering of EC fluxes with a quality control flag of 2 or a friction velocity > 0.2 ms^{-1}, the CO_2 daytime fluxes of the MGA[7] showed excellent agreement with the CO_2 fluxes of the IRGASON which is unaffected by the geometry of the MGA[7] inlet (linear fit with slope 0.98, offset 0.07 $\mu mol\, m^{-2}\, s^{-1}$, $r^2 = 0.96$, and a mean bias of 0.2 $\mu mol\, m^{-2}\, s^{-1}$). With the respective high-frequency corrections, the MGA[7] proved suitable for measuring turbulent CO_2, CO, and NO_x fluxes. We calculated a storage correction from concentration measurements using a single-point profile and estimated random errors based on Finkelstein and Sims (2001). See also Hilland et al. (2025b) and Kunz et al. (2026a) for details on the EC data processing.

For quality control purposes, we applied common EC filters, and discarded measurements lacking well-developed turbulence and stationarity (quality control flag 2 according to Mauder and Foken (2004) or friction velocities $u_* < 0.2\, m\, s^{-1}$), as well as measurements with flow distortion due to the instrument or the tower structure (average wind directions between 340 and 20°N or absolute angle of attack values > 20°). These criteria removed approximately 49 % of the half-hourly flux estimates (Table A.4), with a larger proportion of measurements being removed at night than during the day due to suppressed turbulence at night. Despite the stationarity test considered through the quality control flagging according to Mauder and Foken (2004), some of the retained EC fluxes had extraordinarily large random uncertainties due to large spikes in molar mixing ratios. For CO, these spikes were mostly observed with wind from the southeast, indicating an intermittent, large CO source located upwind in this direction. Since these spikes were generally not correlated with spikes in CO_2 and not adequately captured by the REA measurements (Section 2.1.3), these time periods were not suitable for the proxy-based $ffCO_2$ flux estimation. The same is true for time periods with extraordinarily large or small/negative EC fluxes. Therefore, we also discarded measurements that passed the

Table A.4
Number and percentage of retained half-hourly EC measurements after consecutively applying different quality control and flagging criteria. QC denotes the 0-1-2 quality-control flag according to Mauder and Foken (2004); wind dir denotes the average horizontal wind direction; AoA denotes the angle of attack; u_* denotes the friction velocity; spikes are defined as three or more consecutive concentration measurements (1 min aggregated data) with a median absolute deviation z-score > 7; P0.01 and P0.99 denote the first and 99th percentiles of the respective quality-controlled EC fluxes; blh denotes the boundary layer height from the ERA5 reanalysis estimate (Hersbach et al., 2023); z_{meas} denotes the measurement height; and fp_sum denotes the sum of the flux footprint values modeled in a 15 × 15 km^2 area multiplied by 100, such that fp_sum > 0.8 means that more than 80 % of the observed flux originates from within the modeled area. Lower rows include the application of the quality control criteria listed above. The percentages are given with respect to a total of 11 666 half-hourly time steps between 01 July 2024 and 28 February 2025 (inclusive).

Flagging criteria	Number (percentage) of retained measurements
EC quality control	
QC < 2	7332 (63 %)
20° ≤ wind dir ≤ 340°	7103 (61 %)
| AoA| < 20°	7071 (61 %)
$u_* \geq 0.2\, m\, s^{-1}$	5962 (51 %)
No spikes in CO or NO_x	5769 (49 %)
P0.01 ≤ $F_{CO_2/CO/NO_x}$ ≤ P0.99	5380 (46 %)
Availability of quality-controlled modeled fluxes	
Footprint data available	5347 (46 %)
blh > z_{meas} + 20 m	4421 (38 %)
fp_sum > 0.8	4262 (37 %)
Selected time periods	
Working days	3017 (26 %)
07:00 – 20:00 LT	2140 (18 %)

aforementioned quality control tests, but had large spikes in the CO or NO_x molar mixing ratio time series or CO, NO_x, or CO_2 fluxes below the first or above the 99th percentile of the retained flux values. Similar to the despiking algorithm by Mauder et al. (2013), spikes were defined as three or more consecutive concentration measurements (using 1 min aggregated measurements) with a median absolute deviation z-score > 7. After removal of measurements with extraordinarily large CO or NO_x concentrations and/or CO, NO_x, or CO_2 fluxes below the first or above the 99th percentile, 5380 half-hourly EC data (46 %) were retained (Table A.4). These high- or medium-quality EC data were divided into observations during working days, and observations during Saturdays, Sundays, or public holidays. Due to changes in the human behavior, differences in the magnitude and the temporal patterns of greenhouse gas fluxes and flux ratios were expected between working days and weekend/holidays (e.g., Crawford and Christen, 2015; Karl et al., 2017; Hilland et al., 2025b). As REA measurements were only conducted on working days (Section 2.1.3), we focused on the 3759 half-hourly EC data (32 %) taken on working days. To compare the observations with modeled flux estimates, we only considered time periods for which quality-controlled flux footprints were available (Section 2.1.7). The limited availability of quality-controlled flux footprints reduced the amount of retained data to 3017 half-hourly flux measurements (26 %). 2140 measurements (18 %) were taken on working days between 07:00 and 20:00 LT (Table A.4).

Appendix B. REA-based F_{CO}

Due to failure of the MGA[7] in March 2025, we calculated F_{CO} during the final six REA measurements conducted in March based on the difference in the molar mixing ratio (χ_{CO}) between the updraft and downdraft REA flask samples. In REA, the turbulent flux is given by:

$$F_s = \beta \sigma_w \overline{\rho_m} (\chi_s^{\uparrow} - \chi_s^{\downarrow}), \tag{B.1}$$

where β is an empirical constant, σ_w is the standard deviation of the vertical wind velocity, and $\overline{\rho_m}$ is the mean molar air density (e.g., Rinne et al., 2021). Assuming scalar similarity between CO and CO_2, we calculated β from the EC F_{CO_2} and the flask χ_{CO_2} for each measurement period using Eq. (B.1), in analogy to Eq. (1) for F_{ffCO_2}. We estimated the uncertainty from the REA measurements with available EC F_{CO} data. For these periods, the RMSD, and thus the considered uncertainty, was 0.012 μmol m^{-2} s^{-1}.

Appendix C. Calculation of $\langle R_{CO} \rangle(T_{24h})$ and $\langle R_{NO_x} \rangle$(wind direction)

As the observation-based R_{CO} values generally increased with the average air temperature of the 24 h time period prior to the REA measurements (Fig. 5), we described $\langle R_{CO} \rangle$ as a function of T_{24h}. For this purpose, we divided the 76 REA measurements into five subgroups based on T_{24h}. For each subgroup, we determined the average R_{CO} value using ODR (Fig. 5). In addition, we calculated the average T_{24h} value for each subgroup. Since the ODR considers the uncertainties in F_{CO} and F_{ffCO_2}, we also weighted the average T_{24h} by the uncertainties of the individual F_{CO}/F_{ffCO_2} values. We then fitted a linear function to the $\langle R_{CO} \rangle$ values and the error-weighted T_{24h} values of each subgroup (Fig. C.14). Using this fitted function, we calculated $\langle R_{CO} \rangle$ (in mmol mol^{-1} for each 30 min timestamp depending on T_{24h} (in °C) according to Eq. (C.1).

$$\langle R_{CO} \rangle(T_{24h}) = (0.14 \cdot T_{24h}) + 3.15. \tag{C.1}$$

For NO_x, there was no linear relationship between $\langle R_{NO_x} \rangle$ and $\overline{T_{24h}}$. Since R_{NO_x} was generally higher during southerly winds than during northerly winds (Fig. 6), we defined $\langle R_{NO_x} \rangle$ in mmol mol^{-1} as a function of wind direction according to Eq. (C.2) (compare Fig. 6, Table 2).

$$\langle R_{NO_x} \rangle(\text{wind direction}) = \begin{cases} 1.28 & \text{if } 0° \leq \text{wind direction} < 90° \\ 1.71 & \text{if } 90° \leq \text{wind direction} < 180° \\ 1.85 & \text{if } 180° \leq \text{wind direction} < 270° \\ 1.00 & \text{if } 270° \leq \text{wind direction} < 360° \end{cases} \tag{C.2}$$

Appendix D. Uncertainty estimation of average proxy-based F_{ffCO_2}

To estimate the uncertainties in the proxy-based half-hourly and average F_{ffCO_2} due to the assumption of a constant or temperature-/ wind direction-dependent $\langle R_{proxy} \rangle$ (a), due to the limited number of REA measurements (b), and due to the forcing of the ODR through the origin (c), we calculated the root-mean-square deviation (RMSD) between ^{14}C-based and proxy-based $ffCO_2$ flux estimates during the REA periods, compared observation-based and modeled $\langle R_{proxy} \rangle$, and conducted a synthetic data experiment, where we considered all three uncertainty components (a, b, and c) by simulating the observation-based approach and assuming the inventory-based fluxes as the "truth".

Uncertainty component (a). The uncertainty of the half-hourly, proxy-based F_{ffCO_2}, assuming the REA fluxes were representative of the entire time series (a), could be determined directly from the observations. To this end, we calculated the root-mean-square deviation (RMSD) between the discrete, ^{14}C-based F_{ffCO_2} measured with REA (Eq. (1)) and F_{ffCO_2} estimated as $F_{proxy}/\langle R_{proxy} \rangle$ (Eq. (3)) during the respective measurement periods. This uncertainty is larger than the uncertainty of the direct REA measurements due to contributions from measurement uncertainty and from an unaccounted variability in R_{proxy}. We analyzed the magnitude of these two uncertainty contributions through a synthetic-data experiment. Following Maier et al. (2024a), we calculated for each ^{14}C-based $ffCO_2$ REA flux the corresponding proxy flux, assuming that the observed average ratio $\langle R_{proxy} \rangle$ was "true" and constant. Then, we added random errors to the proxy and $ffCO_2$ fluxes, and divided the error-prone synthetic proxy fluxes again by the ratio $\langle R_{proxy} \rangle$. To mimic real measurements, the random errors were drawn from Gaussian distributions with standard deviations equal to the true average measurement uncertainties during the considered REA sampling periods (0.0084 μmol m^{-2} s^{-1} for F_{CO}, 0.0024 μmol m^{-2} s^{-1} for F_{NO_x}, and 6.5 μmol m^{-2} s^{-1} for F_{ffCO_2}). The RMSD between these synthetic, proxy-based $ffCO_2$ fluxes and the error-prone $ffCO_2$ fluxes provided an estimate of the uncertainty in the proxy-based $ffCO_2$ flux due to measurement uncertainties alone. We attributed the remaining part of the observed RMSD to the unaccounted variability of R_{proxy}. As the RMSD depends on the range of the F_{ffCO_2}, we also computed a normalized RMSD (NRMSD) by dividing the RMSD by the mean F_{ffCO_2}. For details, we refer to an analogous analysis of the uncertainties in proxy-based $ffCO_2$ concentration enhancements in Maier et al. (2024a).

Uncertainty component (b). Since a potential bias in $\langle R_{proxy} \rangle$ calculated from the REA and EC measurements could not be estimated based on observations, we compared $\langle R_{proxy} \rangle$ obtained from an ODR through the modeled proxy and $ffCO_2$ fluxes at the analyzed REA sampling periods with $\langle R_{proxy} \rangle$ obtained from an ODR through the continuous modeled flux time series. Comparing the two modeled $\langle R_{proxy} \rangle$ values provided an estimate of the sampling bias in F_{ffCO_2} (b) based on the modeled variability in R_{proxy}.

Uncertainty components (a), (b), and (c). To estimate the uncertainty in average proxy-based F_{ffCO_2} values, accounting also for measurement uncertainties and bias in average fluxes due to a forced fit through the origin (a, b, and c), we conducted a second synthetic data experiment:

1. To generate a synthetic, continuous measurement record that includes variability in R_{proxy} and measurement uncertainties, we considered the modeled half-hourly F_{ffCO_2} and F_{proxy} values obtained from the convolution of the temporally and spatially resolved emission inventory and flux footprints (Section 2.4) as the "truth", and added random errors representative of actual measurement uncertainties to each modeled flux value.
2. We only considered the time periods during which REA measurements were conducted, as in reality. For simplicity, we used one 30 min value for each measurement instead of averaging the two 30 min values covering the hour-long REA measurements.

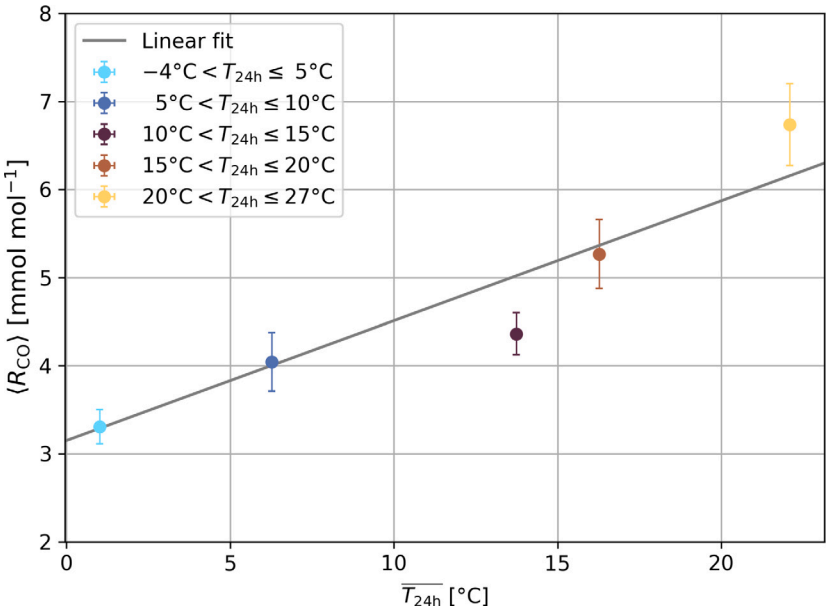


Fig. C.14. Average F_{CO}/F_{ffCO_2} ratio (⟨R_{CO}⟩) obtained from ODRs through five subgroups of REA measurements in dependence of the respective average air temperatures 24 h before the REA sampling period ($\overline{T_{24h}}$). The subgroups were defined based on T_{24h} of each REA measurement. $\overline{T_{24h}}$ was weighted by the uncertainties in R_{CO}, similar to ⟨R_{CO}⟩.

Table D.5
Uncertainty estimates of the average CO- and NO_x-based $ffCO_2$ flux ($\overline{F}_{ffCO_2}$) estimated from the synthetic data experiment. The average standard deviations of the differences between proxy-based and "true" $\overline{F}_{ffCO_2}$ (error bars in Fig. D.15) are given for total, daytime, nighttime, monthly, hourly, and wind-sector-specific averages. Monthly and wind-sector-specific averages include only daytime data. The inventory-based results are given with respect to the average modeled F_{ffCO_2} between 07:00 and 20:00 LT ($\overline{F}_{ffCO_2,day}$ = 18.1 µmol m^{-2} s^{-1}). The absolute uncertainty of the observation-based F_{ffCO_2} estimates was obtained through multiplication with the average observation-based F_{ffCO_2} between 07:00 and 20:00 LT ($\overline{F}_{ffCO_2,day}$ = 12.5 µmol m^{-2} s^{-1}).

Temporal or spatial scale	Relative $\overline{F}_{ffCO_2}$ uncertainty [%]		Absolute $\overline{F}_{ffCO_2}$ uncertainty (obs.) [µmol m^{-2} s^{-1}]	
	CO	NO_x	CO	NO_x
All 30 min periods	20	17	2.5	2.1
07:00–20:00 LT	23	19	2.9	2.4
20:00–07:00 LT	12	10	1.5	1.3
Monthly	23	19	2.8	2.4
Hourly	35	26	4.4	3.2
Per wind sector	24	20	2.9	2.5

3. For these selected timestamps, we determined the average $F_{proxy}F_{ffCO_2}$ ratio by ODR forced through the origin.
4. By dividing the average error-prone proxy flux by this average ratio ⟨R_{proxy}⟩, we determined the synthetic proxy-based average $ffCO_2$ flux, representing our observation-based approach.

In the synthetic data experiment, the uncertainty of the average proxy-based F_{ffCO_2} could thus be determined by comparing this synthetic, proxy-based average $ffCO_2$ flux with the "true" average F_{ffCO_2}. To obtain a statistically representative uncertainty, we repeated the experiment 10 000 times. In each experiment, the random flux uncertainties representing the measurement uncertainties changed, while the "true" fluxes and the timestamps used in the ODR remained constant. We then calculated the standard deviation of the 10 000 synthetic uncertainty estimates to obtain an estimate of the uncertainty in average, proxy-based $ffCO_2$ fluxes. Since the standard deviation (in µmol m^{-2} s^{-1}) depends on the magnitude of the modeled fluxes, we divided the standard deviation by the average modeled $ffCO_2$ flux of the quality-controlled data between 07:00 and 20:00 LT to scale the uncertainty back to the observation-based flux estimates. The data experiment also provided an estimate of the bias in the average F_{ffCO_2} caused by the non-linearity of dividing F_{proxy} by ⟨R_{proxy}⟩ and the sampling bias. Bias and uncertainty in monthly, hourly, or wind direction-dependent average F_{ffCO_2} estimates were obtained analogously by comparing the "true" and synthetic, proxy-based average fluxes for each time period or wind sector.

Considering all quality-controlled 30 min data, the average difference between the synthetic proxy-based F_{ffCO_2} and the "true" F_{ffCO_2} was −10 ± 20 % for the CO-based approach and −7 ± 17 for the NO_x-based approach (Fig. D.15a, Table D.5). When considering only data between 07:00 and 20:00 LT, the bias reduced to −4 % and −0.6 %, respectively. For nighttime data, the differences between the synthetic proxy-based and direct F_{ffCO_2} were −25 % and −23 %. As F_{proxy}/F_{ffCO_2} ratios were determined from the (daytime) REA measurement periods, during which the flux contribution from road transport was generally higher than at night, the proxy-based $ffCO_2$ flux estimates were more accurate during the day than at night. The underestimation of F_{ffCO_2} between 07:00 and 20:00 LT was also evident in the hourly averages (Fig. D.15c). The average uncertainty of the hourly averages was 35 % for the CO-based approach and 26 % for the NO_x-based approach.

Using a constant F_{proxy}/F_{ffCO_2} ratio, proxy-based F_{ffCO_2} estimates were up to 37 % too high from July to October, and up to 46 % too low from November to February (Fig. D.15b). The difference was slightly larger for CO than for NO_x, as the difference between R_{CO} of road transport and R_{CO} of stationary combustion was larger for CO than for NO_x. The standard deviation of the monthly $\Delta\overline{F}_{ffCO_2}$ was on average 23 % for the CO-based F_{ffCO_2} and 19 % for the NO_x-based F_{ffCO_2}.

Due to slightly higher F_{proxy}/F_{ffCO_2} ratios in the south than in the north, proxy-based F_{ffCO_2} estimates using a constant F_{proxy}/F_{ffCO_2} ratio were underestimated in the northeast by about 16 % and overestimated in the southwest by 8 % for COand 18 % for NO_x. The average standard deviation of the synthetic $\Delta\overline{F}_{ffCO_2}$ for each wind sector was 24 % for the CO-based approach and 20 % for the NO_x-based approach.

Based on the average standard deviations of the differences between proxy-based and "true" F_{ffCO_2} estimates (error bars in Fig. D.15), we assumed an uncertainty of about 20 % for total, daytime, monthly, and wind sector specific averages, and about 30 % for monthly averages (Table D.5). Although the synthetic data experiment reflected the assumption of one constant ⟨R_{proxy}⟩ value, we used the estimated relative

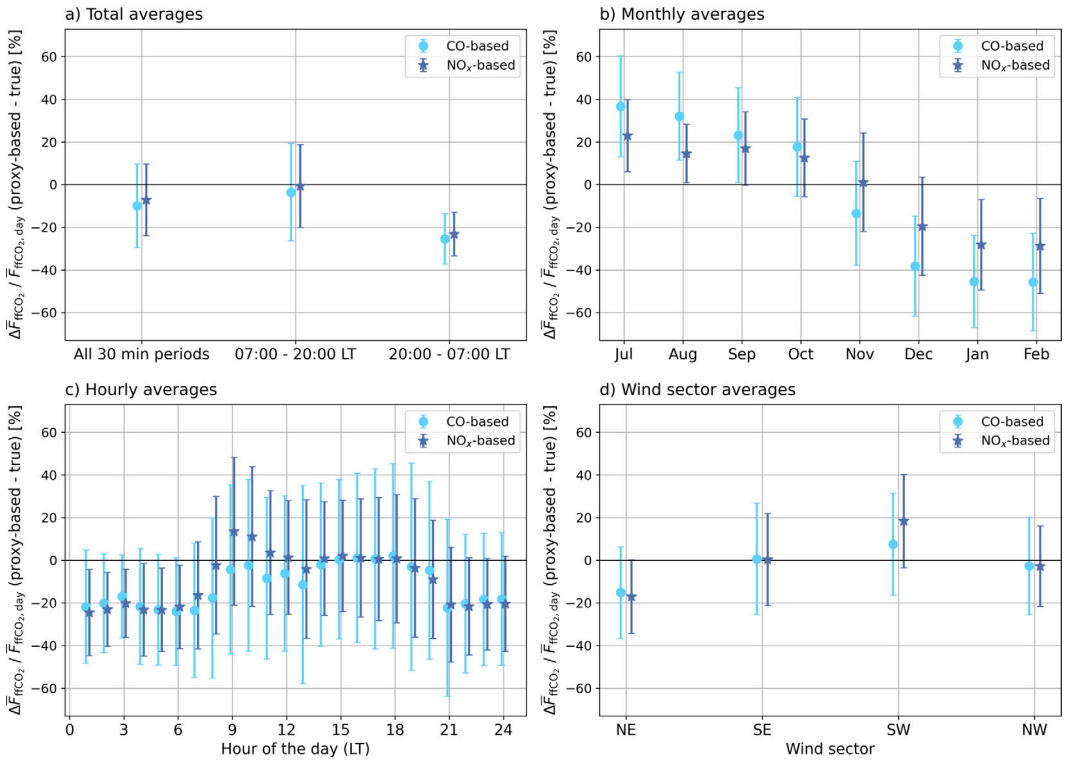


Fig. D.15. Results from a synthetic data experiment used to estimate the uncertainty of average proxy-based $\mathrm{ffCO_2}$ fluxes. Shown is the relative difference between the average inventory-based $\mathrm{ffCO_2}$ flux ("true") and the average $\mathrm{ffCO_2}$ flux calculated from an error-prone inventory-based proxy flux and an average $F_{\mathrm{proxy}}/F_{\mathrm{ffCO_2}}$ ratio obtained from error-prone inventory-based fluxes. The data points and error bars represent the means and standard deviations from 10 000 repetitions of the experiment. The results are given with respect to the average modeled $F_{\mathrm{ffCO_2}}$ between 07:00 and 20:00 LT ($\overline{F}_{\mathrm{ffCO_2,day}} = 18.1\,\mu\mathrm{mol\,m^{-2}\,s^{-1}}$). In (b), (c), and (d), only data between 07:00 and 20:00 LT was considered.

uncertainty also for the approach with wind direction- or temperature-dependent flux ratios. These approaches should only decrease the uncertainty and the bias, if at all. In our study, an independent measure of bias in $F_{\mathrm{ffCO_2}}$ was the difference between CO- and NO_x-based $F_{\mathrm{ffCO_2}}$ estimates.

Appendix E. Source sector contributions to modeled fluxes

See Table E.6 and Fig. E.16.

Appendix F. Comparison of modeled flux estimates using HBEFA 4.2 and HBEFA 5.1 emission factors

The latest emissions inventory data used in this study (Version 2.6.0) were the result of several updates and improvements based partly on identified discrepancies between the modeled and observation-based flux estimates, which have repeatedly improved their agreement. Independent of observation-based results, Version 2.6.0 involved updating the HBEFA emission factors used to calculate road transport emissions from Version 4.2 to 5.1. This update substantially extended the contents compared to HBEFA 4.2, including new vehicle types and processes (Notter et al., 2026). With the update of the HBEFA factors, the annual emissions from road transport within the administrative boundary of the city of Munich increased by 10 % for $\mathrm{CO_2}$, by 7 % for $\mathrm{nfCO_2}$, by 19 % for NO_x, and by 102 % for CO. While the footprint-averaged $\mathrm{CO_2}$ and NO_x fluxes, and $F_{\mathrm{NO}_x}/F_{\mathrm{ffCO_2}}$ ratios increased only slightly, the increase in modeled F_{CO}, and thus in the $F_{\mathrm{CO}}/F_{\mathrm{ffCO_2}}$ ratio, was substantial (Fig. F.17). While the average modeled R_{CO} agreed better with the average observation-based R_{CO} with HBEFA 4.2, the modeled CO emissions with HBEFA 4.2 were even more dominated by the emissions from off-road transport (40 %). Due to the substantial uncertainties in the modeled off-road emissions, and given that the observation-based R_{CO} values were often higher than $\langle R_{\mathrm{CO}} \rangle$ from road transport, the REA measurements suggested that $\langle R_{\mathrm{CO}} \rangle$ was underestimated in HBEFA 4.2. Similarly, an underestimation of $\langle R_{\mathrm{NO}_x} \rangle$ from road transport in the emission inventory was suggested. The higher emission ratios in HBEFA 5.1 were therefore consistent with previous findings. A more quantitative evaluation of the emission ratios of road transport remained limited by the substantial CO contribution from off-road emissions (40 % with HBEFA 4.2, 28 % with HBEFA 5.1). The substantial changes resulting from an update of emission factors highlights the importance of an observation-based evaluations of emissions and emission ratios.

Appendix G. Average $\mathrm{nfCO_2}$ fluxes in dependence of air temperature for easterly fluxes

See Fig. G.18.

Data availability

The VPRM model results for 2024 and 2025 are available upon request. All other datasets used in the present study are available in the ICOS Cities Data Portal or a Zenodo repository under Creative Commons Licence CC-BY-4.0:

- Relaxed eddy accumulation dataset Kunz et al. (2025a)
- Eddy covariance dataset: Hilland et al. (2025a)
- Flux footprints and turbulence data used: Molinier and Kljun (2026), ICOS Ecosystem Thematic Centre et al. (2025)
- Munich emission inventory (annual means and temporal profiles): Aigner et al. (2025), Kühbacher et al. (2026a,b)
- Observation-based and modeled flux estimates as well as meteorological data and quality control flags at half-hourly resolution: Kunz et al. (2026b)

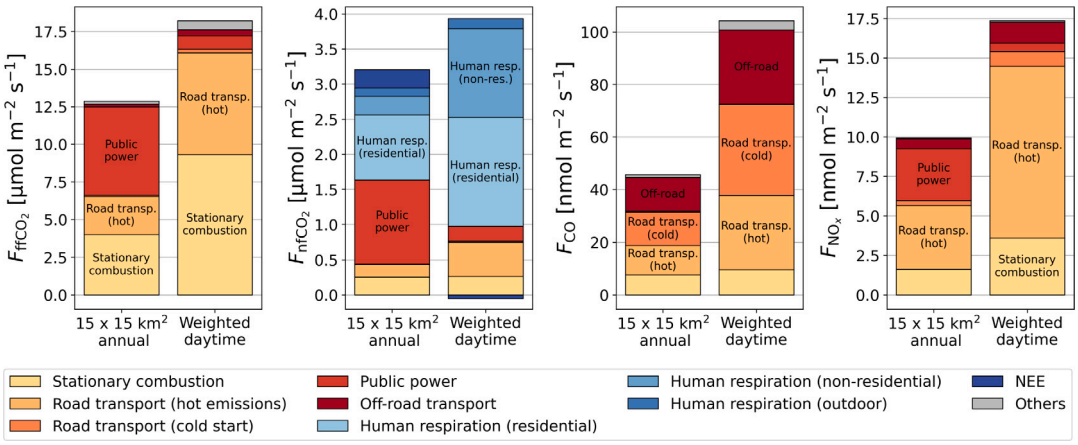


Fig. E.16. Average $ffCO_2$, $nfCO_2$, CO, and NO_x fluxes. For each gas, the annual average within the 15 × 15 km^2 footprint domain for the year 2024 and the daytime average of the footprint-weighted modeled fluxes, as presented in Table E.6, are given. To avoid overrepresentation of time periods with more available data (Fig. 3b), the footprint-weighted fluxes were first averaged per hour, then averaged over all hours. "Others" comprises the sectors fugitives, solvents, shipping, waste, agri-livestock, and agri-others.

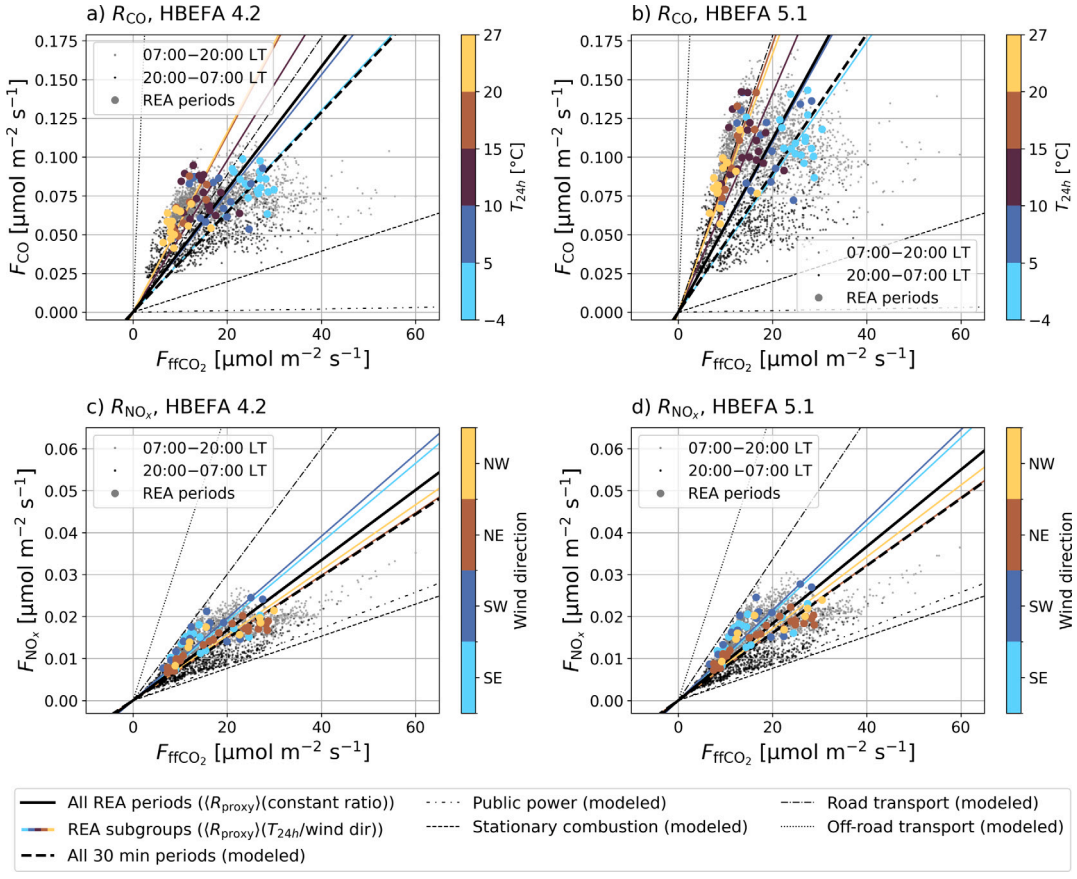


Fig. F.17. Comparison of the modeled F_{proxy} and F_{ffCO_2} at the measurement site using HBEFA emission factors 4.2 (a, c) and 5.1 (b, d). Solid lines illustrate the orthogonal distance regressions (ODR) for all data points and the respective temperature-based subgroups. The slopes of the dashed lines represent the average flux ratios of the dominant source sectors. For clarity, individual data points with modeled F_{ffCO_2} up to 140 µmol m^{-2} s^{-1} were omitted.

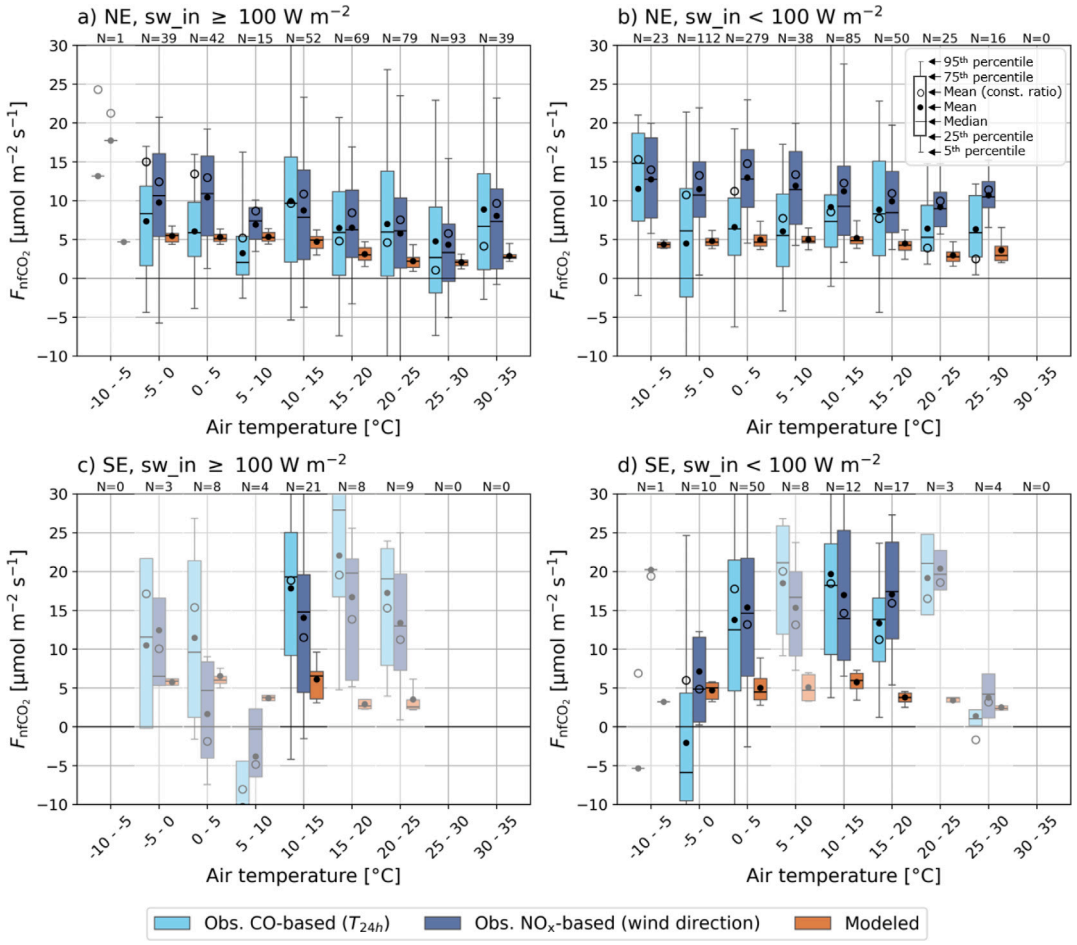


Fig. G.18. $F_{\mathrm{nfCO_2}}$ in dependence on air temperature during the 30 min averaging intervals. (a) and (c) include timestamps when the downwelling shortwave radiation (sw_in) was ≥100 W m^{-2}, while (b) and (d) include timestamps when sw_in was <100 W m^{-2} for the northeast and southeast wind sectors, respectively. The sw_in <100 W m^{-2} category includes nighttime data. Data with $N < 10$ is shown in faded colors.

Table E.6
Absolute fluxes and relative flux contributions to the inventory- and VPRM-based $ffCO_2$, $nfCO_2$, CO, and NO_x fluxes per source sector. Given are the annual averages within the 15 × 15 km^2 footprint domain and, in parentheses, the averages of the modeled, footprint-weighted daytime fluxes, as presented in Figs. 8, 9, and 12a. To avoid overrepresentation of time periods with more available data (Fig. 3b), the footprint-weighted fluxes were first averaged per hour, then averaged over all hours. Relative contributions <0.5 % were omitted for clarity ("–"). For the sectors shipping, waste, AgriLivestock, and AgriOther, the contributions were <0.5 % for all gases.

Sector	$ffCO_2$	$nfCO_2$	CO	NO_x
Absolute fluxes [$\mu mol\ m^{-2}\ s^{-1}$]				
All sectors	13 (18)	3 (4)	0.05 (0.10)	0.099 (0.017)
Relative flux contributions [%]				
Public power	46 (5)	37 (5)	1 (0)	33 (3)
Stat. combustion	31 (51)	8 (7)	17 (9)	16 (21)
Road transp. (hot)	20 (37)	6 (13)	25 (27)	41 (63)
Road transp. (cold)	1 (1)	–	28 (33)	3 (5)
Off-road	1 (2)	–	28 (27)	6 (8)
Fugitive	1 (1)	–	–	–
Solvents	1 (3)	–	2 (4)	–
Human respiration	–	42 (76)	–	–
NEE	–	8 (–1)	–	–

References

Abolhasani, S., Frey, H.C., Kim, K., Rasdorf, W., Lewis, P., Pang, S.H., 2008. Real-world in-use activity, fuel use, and emissions for nonroad construction vehicles: a case study for excavators. J. Air Waste Manage. Assoc. 58, 1033–1046. http://dx.doi.org/10.3155/1047-3289.58.8.1033.

Aigner, P., Chen, J., Althammer, T., Denier van der Gon, H., Harter, H., Günther, M., Kühbacher, D., Suhendra, M., Super, I., Yirtar, B., Zinsmeister, D., 2026. Munich CO_2 emission inventory for sectors public power and commercial and residential stationary combustion for the years 2019–2024. Atmos. Env.: X 31, 100498. http://dx.doi.org/10.1016/j.aeaoa.2026.100498.

Aigner, P., Kühbacher, D., Chen, J., Althammer, T., Denier van der Gon, H., Hinderer, J., Suhendra, M., Super, I., Yirtar, B., 2025. Temporal activity profiles for the City of Munich (2019–2024). http://dx.doi.org/10.18160/Z2CB-JKQ2.

Brunner, D., Suter, I., Bernet, L., Constantin, L., Grange, S.K., Rubli, P., Li, J., Chen, J., Bigi, A., Emmenegger, L., 2025. Building-resolving simulations of anthropogenic and biospheric CO_2 in the city of Zurich with GRAMM/GRAL. Atmos. Chem. Phys. 25, 14387–14410. http://dx.doi.org/10.5194/acp-25-14387-2025.

Chen, J., Viatte, C., Hedelius, J.K., Jones, T., Franklin, J.E., Parker, H., Gottlieb, E.W., Wennberg, P.O., Dubey, M.K., Wofsy, S.C., 2016. Differential column measurements using compact solar-tracking spectrometers. Atmos. Chem. Phys. 16, 8479–8498. http://dx.doi.org/10.5194/acp-16-8479-2016.

Christen, A., 2014. Atmospheric measurement techniques to quantify greenhouse gas emissions from cities. Urban Clim. 10, 241–260. http://dx.doi.org/10.1016/j.uclim.2014.04.006.

Christen, A., Coops, N.C., Crawford, B.R., Kellett, R., Liss, K.N., Olchovski, I., Tooke, T.R., van der Laan, M., Voogt, J.A., 2011. Validation of modeled carbon-dioxide emissions from an urban neighborhood with direct eddy-covariance measurements. Atmos. Environ. 45, 6057–6069. http://dx.doi.org/10.1016/j.atmosenv.2011.07.040.

Crameri, F., 2023. Scientific colour maps. http://dx.doi.org/10.5281/zenodo.8409685.

Crameri, F., Shephard, G.E., Heron, P.J., 2020. The misuse of colour in science communication. Nat. Commun. 11, 5444. http://dx.doi.org/10.1038/s41467-020-19160-7.

Crawford, B., Christen, A., 2015. Spatial source attribution of measured urban eddy covariance CO_2 fluxes. Theor. Appl. Climatol. 119, 733–755. http://dx.doi.org/10.1007/s00704-014-1124-0.

Dröge, R., Denier van der Gon, H., Perrussel, O., David, L., Aigner, P., Kuehbacher, D., Chen, J., Hinderer, J., Brunner, D., Constantin, L., 2024. Final version of high-resolution city emission inventory for GHGs and co-emitted species for 2018, 2020 and 2022. http://dx.doi.org/10.18160/0GEF-R5XX.

Fasano, E., Matthews, B., Vuolo, F., Schume, H., 2026. Comparing local CO_2 emission inventories with tall tower flux measurements in Vienna, Austria. Atmos. Env.: X 30, 100443. http://dx.doi.org/10.1016/j.aeaoa.2026.100443.

Feigenwinter, C., Vogt, R., Christen, A., 2012. Eddy covariance measurements Over Urban Areas. In: Aubinet, M., Vesala, T., Papale, D. (Eds.), Eddy Covariance. Springer, Dordrecht, pp. 377–398. http://dx.doi.org/10.1007/978-94-007-2351-1_16.

Finkelstein, P.L., Sims, P.F., 2001. Sampling error in eddy correlation flux measurements. J. Geophys. Res.: Atmos. 106, 3503–3509. http://dx.doi.org/10.1029/2000JD900731.

Foken, T., Göckede, M., Mauder, M., Mahrt, L., Amiro, B., Munger, W., 2004. Post-field data quality control. In: Lee, X., Massman, W., Law, B. (Eds.), Handbook of Micrometeorology. In: Atmospheric and Oceanographic Sciences Library, vol. 29, Springer, Dordrecht, pp. 181–208. http://dx.doi.org/10.1007/1-4020-2265-4_9.

Fotiadi, A.K., Lohou, F., Druilhet, A., Sera, D., Brunet, Y., Delmas, R., 2005. Methodological development of the conditional sampling method. Part I: Sensitivity to statistical and technical characteristics. Bound.-Layer Meteorol. 114, 615–640. http://dx.doi.org/10.1007/s10546-004-1080-9.

Fratini, G., Ibrom, A., Arriga, N., Burba, G., Papale, D., 2012. Relative humidity effects on water vapour fluxes measured with closed-path eddy-covariance systems with short sampling lines. Agricult. Forest Meteorol. 165, 53–63. http://dx.doi.org/10.1016/j.agrformet.2012.05.018.

Gurney, K.R., Liang, J., Patarasuk, R., O'Keeffe, D., Huang, J., Hutchins, M., Lauvaux, T., Turnbull, J.C., Shepson, P.B., 2017. Reconciling the differences between a bottom-up and inverse-estimated $FFCO_2$ emissions estimate in a large US urban area. Elem.: Sci. Anthr. 5, http://dx.doi.org/10.1525/elementa.137.

Hersbach, H., Bell, B., Berrisford, P., Biavati, G., Horányi, A., Muñoz Sabater, J., Nicolas, J., Peubey, C., Radu, R., Rozum, I., Schepers, D., Simmons, A., Soci, C., Dee, D., Thépaut, J.N., 2023. ERA5 hourly data on single levels from 1940 to present. http://dx.doi.org/10.24381/cds.adbb2d47.

Hilland, R., Hammer, S., Holst, C., Kunz, A.K., Lan, C., Mauder, M., Zeeman, M., Christen, A., 2025a. EC flux time series archive (L2), Oberpostdirektion, 2024-06-28–2025-02-28. http://dx.doi.org/10.18160/CFHP-RY4X.

Hilland, R., Hashemi, J., Stagakis, S., Brunner, D., Constantin, L., Kljun, N., Kunz, A.K., Molinier, B., Hammer, S., Emmenegger, L., Christen, A., 2025b. Sectoral attribution of greenhouse gas and pollutant emissions using multi-species eddy covariance on a tall tower in Zurich, Switzerland. Atmos. Chem. Phys. 25, 14279–14299. http://dx.doi.org/10.5194/acp-25-14279-2025.

ICOS Ecosystem Thematic Centre, Holst, C., Lan, C., Jahn, C., Christen, A., Hilland, R., Stagakis, S., Nicolini, G., Mauder, M., 2025. ETC L2 fluxes from Oberpostdirektion, 2022-12-31–2026-03-31, ICOS cities. URL https://hdl.handle.net/11676/HyC8aZLr8BoB5JH7j_AnbNWt.

Juchem, H., Maier, F., Levin, I., Jordan, A., Pöhler, D., Rosendahl, C., Della Coletta, J., Preunkert, S., Hammer, S., 2025. Challenges and benefits of using NO_x as a quantitative proxy for fossil fuel CO_2 in an urban area based on radiocarbon measurements. Atmos. Chem. Phys. 25, 18373–18388. http://dx.doi.org/10.5194/acp-25-18373-2025.

Kaimal, J.C., Wyngaard, J.C., Izumi, Y., Coté, O.R., 1972. Spectral characteristics of surface–layer turbulence. Q. J. R. Meteorol. Soc. 98, 563–589. http://dx.doi.org/10.1002/qj.49709841707.

Karl, T., Graus, M., Striednig, M., Lamprecht, C., Hammerle, A., Wohlfahrt, G., Held, A., von der Heyden, L., Deventer, M.J., Krismer, A., Haun, C., Feichter, R., Lee, J., 2017. Urban eddy covariance measurements reveal significant missing NO_x emissions in Central Europe. Sci. Rep. 7, 2536. http://dx.doi.org/10.1038/s41598-017-02699-9.

Kljun, N., Calanca, P., Rotach, M.W., Schmid, H.P., 2015. A simple two-dimensional parameterisation for Flux Footprint Prediction (FFP). Geosci. Model. Dev. 8, 3695–3713. http://dx.doi.org/10.5194/gmd-8-3695-2015.

Kühbacher, D., Aigner, P., Chen, J., Hinderer, J., Suhendra, M., Yirtar, B., Super, I., Denier van der Gon, H., Dröge, R., Schoenecker, E., Hohenberger, T., 2026a. Munich city inventory. URL https://github.com/tum-esm/tum-mci/. (Last Access: 30 June 2026).

Kühbacher, D., Aigner, P., Chen, J., Hinderer, J., Super, I., Denier van der Gon, H., Dröge, R., Schoenmakers, E., Hohenberger, T., 2026b. Gridded anthropogenic emissions of CO_2, CH_4 and co-emitted pollutants for the city of Munich in 2024, 2024-01-01–2024-12-31, ICOS cities. URL https://hdl.handle.net/11676/n6kESXJk3Va_ylZG_ai8qNBJ. (Last Access: 30 June 2026).

Kühbacher, D., Chen, J., Aigner, P., Ilic, M., Super, I., Denier van der Gon, H., 2025. DRIVE v1.0: a data-driven framework to estimate road transport emissions and temporal profiles. Geosci. Model. Dev. 18, 9967–9990. http://dx.doi.org/10.5194/gmd-18-9967-2025.

Kunz, A.K., Aigner, P., Becker, C., Borchardt, L., Chen, J., Christen, A., Della Coletta, J., Eritt, M., Gutiérrez, X., Hashemi, J., Hilland, R., Holst, C., Jahn, C., Jordan, A., Kneißl, R., Kürzinger, K., Lan, C., Legendre, V., Levin, I., Mauder, M., Preunkert, S., Hammer, S., 2025a. REA flux time series archive (L2) from Oberpostdirektion. http://dx.doi.org/10.18160/98S6-A1N8.

Kunz, A.K., Borchardt, L., Christen, A., Della Coletta, J., Eritt, M., Gutiérrez, X., Hashemi, J., Hilland, R., Jordan, A., Kneißl, R., Legendre, V., Levin, I., Preunkert, S., Rubli, P., Stagakis, S., Hammer, S., 2025b. A relaxed eddy accumulation flask sampling system for ^{14}C-based partitioning of fossil and non-fossil CO_2 fluxes. Atmos. Meas. Tech. 18, 5349–5373. http://dx.doi.org/10.5194/amt-18-5349-2025.

Kunz, A.K., Hammer, S., Aigner, P., Bignotti, L., Borchardt, L., Chen, J., Della Coletta, J., Emmenegger, L., Eritt, M., Gutiérrez, X., Hashemi, J., Hilland, R., Holst, C., Jordan, A., Kljun, N., Kneißl, R., Lan, C., Legendre, V., Levin, I., Loubet, B., Mauder, M., Molinier, B., Preunkert, S., Ramonet, M., Stagakis, S., Christen, A., 2026a.^{14}C-based separation of fossil and non-fossil CO_2 fluxes in cities using relaxed eddy accumulation: results from tall-tower measurements in Zurich, Paris, and munich. Atmos. Chem. Phys. 26, 4967–5003. http://dx.doi.org/10.5194/acp-26-4967-2026.

Kunz, A.K., Hammer, S., Aigner, P., Borchardt, L., Chen, J., Della Coletta, J., Eritt, M., Friedrich, R., Gutiérrez, X., Hilland, R., Holst, C., Jordan, A., Kljun, N., Kneißl, R., Kühbacher, D., Lan, C., Li, J., Molinier, B., Preunkert, S., Christen, A., 2026b. Data supporting the manuscript "continuous fossil fuel CO_2 emission estimates based on ^{14}C-calibrated urban eddy-covariance fluxes of co-emitted species". http://dx.doi.org/10.5281/zenodo.20622757.

Lan, C., Mauder, M., Stagakis, S., Loubet, B., D'Onofrio, C., Metzger, S., Durden, D., Herig-Coimbra, P.H., 2024. Intercomparison of eddy-covariance software for urban tall-tower sites. Atmos. Meas. Tech. 17, 2649–2669. http://dx.doi.org/10.5194/amt-17-2649-2024.

Lee, J.D., Helfter, C., Purvis, R.M., Beevers, S.D., Carslaw, D.C., Lewis, A.C., Møller, S.J., Tremper, A., Vaughan, A., Nemitz, E.G., 2015. Measurement of NO_x fluxes from a tall tower in Central London, UK and comparison with emissions inventories. Environ. Sci. Technol. 49, 1025–1034. http://dx.doi.org/10.1021/es5049072.

Levin, I., Kromer, B., Schmidt, M., Sartorius, H., 2003. A novel approach for independent budgeting of fossil fuel CO_2 over Europe by $^{14}CO_2$ observations. Geophys. Res. Lett. 30, http://dx.doi.org/10.1029/2003GL018477.

Li, J., Chen, J., Glauch, T., Brunner, D., Marshall, J., Ponomarev, N., Tang, H., Stagakis, S., 2026. Fine–scale estimation of urban biogenic CO_2 fluxes: A novel framework integrating multiple versions of vegetation photosynthesis and respiration models and in situ measurements. Earth's Futur. 14, http://dx.doi.org/10.1029/2025EF007458.

Maier, F., Levin, I., Conil, S., Gachkivskyi, M., Denier van der Gon, H., Hammer, S., 2024a. Uncertainty in continuous ΔCO-based $\Delta ffCO_2$ estimates derived from ^{14}C flask and bottom-up $\Delta CO/\Delta ffCO_2$ ratios. Atmos. Chem. Phys. 24, 8205–8223. http://dx.doi.org/10.5194/acp-24-8205-2024.

Maier, F., Levin, I., Gachkivskyi, M., Rödenbeck, C., Hammer, S., 2023. Estimating regional fossil fuel CO_2 concentrations from $^{14}CO_2$ observations: challenges and uncertainties. Philos. Trans. A 381, 20220203. http://dx.doi.org/10.1098/rsta.2022.0203.

Maier, F., Rödenbeck, C., Levin, I., Gerbig, C., Gachkivskyi, M., Hammer, S., 2024b. Potential of ^{14}C-based vs. ΔCO-based $\Delta ffCO_2$ observations to estimate urban fossil fuel CO_2 ($ffCO_2$) emissions. Atmos. Chem. Phys. 24, 8183–8203. http://dx.doi.org/10.5194/acp-24-8183-2024.

Mauder, M., Cuntz, M., Drüe, C., Graf, A., Rebmann, C., Schmid, H.P., Schmidt, M., Steinbrecher, R., 2013. A strategy for quality and uncertainty assessment of long-term eddy-covariance measurements. Agricult. Forest Meteorol. 169, 122–135. http://dx.doi.org/10.1016/j.agrformet.2012.09.006.

Mauder, M., Foken, T., 2004. Documentation and instruction manual of the eddy-covariance software package TK2. Arbeitsergebnisse Univ. Bayreuth. Abt. Mikrometeorol. (ISSN: 1614-8924) 26.

Molinier, B., Aigner, P., Brunner, D., Chen, J., Christen, A., Constantin, L., Denier van der Gon, H., Hilland, R., Kühbacher, D., Li, J., Maiwald, R., Super, I., Vardag, S.N., Kljun, N., 2026. Insights from the convolution of emission inventories with flux footprints from tall eddy covariance towers at three European cities. ACS EST Air http://dx.doi.org/10.1021/acsestair.6c00148.

Molinier, B., Kljun, N., 2024. Footprints for the flux towers in three pilot cities: Deliverable 2.6. Project number 101037319. http://dx.doi.org/10.18160/9VPH-CA6E.

Molinier, B., Kljun, N., 2026. Munich-Oberpostdirektion flux footprints. http://dx.doi.org/10.18160/HN4Q-PK8X.

Moncrieff, J., Clement, R., Finnigan, J., Meyers, T., 2004. Averaging, detrending, and filtering of eddy covariance time series. In: Lee, X., Massman, W., Law, B. (Eds.), Handbook of Micrometeorology. In: Atmospheric and Oceanographic Sciences Library, Springer, Dordrecht, pp. 7–31. http://dx.doi.org/10.1007/1-4020-2265-4_2.

Notter, B., Cox, B., Hausberger, S., Matzer, C., Weller, K., Dippold, M., Politschnig, N., Lipp, S., Allekotte, M., Knörr, W., Andre, M., Gangnepain, L., Hult, C., Jerskjö, M., 2022. HEBFA 4.2 documentation of updates, update report. URL https://cdn.prod.website-files.com/6207922a2acc01004530a67e/6217584903e9f9b63093c8c0_HBEFA42_Update_Documentation.pdf. (Last Access: 16 June 2026).

Notter, B., Cox, B., Weller, K., Opetnik, M., Dippold, M., Hausberger, S., Present, S., Heidt, C., Kräck, J., Allekotte, M., Knörr, W., André, M., Vansevenant, B., Liu, Y., Berdica, K.V., Sahlgren, T., Sjödin, A., Priestley, M., Jerksjö, M., Hult, C., Engedal, M., Storbraten, B., Borken-Kleefeld, J., Kumawat, P., Potturu, L., 2026. HBEFA 5.1 documentation of updates. URL https://download.hbefa.net/reports/hb51/HBEFA5.1_Update_documentation_v1.1_2026-02-13.pdf. (Last Access: 16 June 2026).

Rebmann, C., Kolle, O., Heinesch, B., Queck, R., Ibrom, A., Aubinet, M., 2012. Data acquisition and flux calculations. In: Aubinet, M., Vesala, T., Papale, D. (Eds.), Eddy Covariance. Springer, Dordrecht, pp. 59–84. http://dx.doi.org/10.1007/978-94-007-2351-1_3.

Rinne, J., Ammann, C., Pattey, E., Paw U., K.T., Desjardins, R.L., 2021. Alternative turbulent trace gas flux measurement methods. In: Foken, T. (Ed.), Springer Handbook of Atmospheric Measurements. In: Springer Handbooks, Springer, Cham, pp. 1505–1530. http://dx.doi.org/10.1007/978-3-030-52171-4_56.

Rosendahl, C.L., 2022. Proxy to Fossil-Fuel Co_2 Emission Ratios: In-Situ Versus Inventory Data (Ph.D. thesis). Heidelberg University, http://dx.doi.org/10.11588/heidok.00031909.

Rosendahl, C., Alberti, C., Hase, F., Hammer, S., 2022. Source sector dominated proxy/$ffCO_2$ ratios. URL https://verify.lsce.ipsl.fr/images/PublicDeliverables/VERIFY_D28_final-v1.pdf. (Last Access: 14 March 2026).

Stagakis, S., Brunner, D., Li, J., Backman, L., Karvonen, A., Constantin, L., Järvi, L., Havu, M., Chen, J., Emberger, S., Kulmala, L., 2025. Intercomparison of biogenic CO_2 flux models in four urban parks in the city of Zurich. Biogeosci. 22, 2133–2161. http://dx.doi.org/10.5194/bg-22-2133-2025.

Stagakis, S., Feigenwinter, C., Vogt, R., Brunner, D., Kalberer, M., 2023a. A high-resolution monitoring approach of urban CO_2 fluxes. Part 2 - surface flux optimisation using eddy covariance observations. Sci. Total Environ. 903, 166035. http://dx.doi.org/10.1016/j.scitotenv.2023.166035.

Stagakis, S., Feigenwinter, C., Vogt, R., Kalberer, M., 2023b. A high-resolution monitoring approach of urban CO_2fluxes. Part 1 - bottom-up model development. Sci. Total Environ. 858, 160216. http://dx.doi.org/10.1016/j.scitotenv.2022.160216.

Statistisches Amt München, 2026. Bevölkerung 2000 - 2025 nach Geschlecht und Staatsangehörigkeit. URL https://stadt.muenchen.de/dam/jcr:c45700b2-e2c3-4d66-99fa-55e4c77ab3ee/jt260101.pdf. (Last Access: 28 August 2026).

Stuiver, M., Polach, H.A., 1977. Discussion reporting of ^{14}C data. Radiocarbon 19, 355–363. http://dx.doi.org/10.1017/S0033822200003672.

Super, I., Brunner, D., Perrussel, O., Kühbacher, D., Aigner, P., Yirtar, B., Suhendra, M., Chen, J., 2023. Temporally varying city emission inventory for GHGs and co-emitted species for 2021. URL https://fileshare.icos-cp.eu/s/AAnMdZR8efs6CBD. (Last Access: 30 June 2026).

Turnbull, J.C., Curras, T., Gurney, K.R., Hilton, T.W., Mueller, K.L., Vogel, F., Yao, B., Albarus, I., Ars, S., Baidar, S., Chatterjee, A., Chen, H., Chen, J., Christen, A., Davis, K.J., Hajny, K., Han, P., Karion, A., Kim, J., Lopez Coto, I., Papale, D., Ramonet, M., Sperlich, P., Vardag, S.N., Vermeulen, A., Vimont, I.J., Wu, D., Zhang, W., Augusti-Panareda, A., Ahlgren, K., Ahn, D., Boyle, T., Brewer, A., Brunner, D., Cai, Q., Chambers, S., Chen, Z., Dadheech, N., D'Onofrio, C., Dunse, B.L., Engelen, R., Fathi, S., Gioli, B., Hammer, S., Hase, F., Hong, J., Hutyra, L.R., Järvi, L., Jeong, S., Karstens, U., Kenion, H.C., Kljun, N., Laurent, O., Lauvaux, T., Lin, J.C., Liu, Z., Loh, Z., Maier, F., Matthews, B., Mauder, M., Miles, N., Mitchell, L., Monteiro, V.C., Mostafavi Pak, N., Röckmann, T., Roiger, A., Roten, D., Scheutz, C., Shahrokhi, N., Shepson, P.B., Stagakis, S., Tong, X., Trudinger, C.M., Velasco, E., Whetstone, J.R., Winbourne, J.B., Wu, J., Xueref-Remy, I., Yadav, V., Yu, L., Zazzeri, G., Zeng, N., Zhou, M., 2025. IG3IS urban greenhouse gas emission observation and monitoring good research practice guidelines WMO GAW report 314. http://dx.doi.org/10.59327/WMO/GAW/314.

Turnbull, J.C., Graven, H., Krakauer, N.Y., 2016. Radiocarbon in the atmosphere. In: Schuur, E.A., Druffel, E.R.M., Trumbore, S.E. (Eds.), Radiocarbon and Climate Change. Springer, Cham, pp. 83–137. http://dx.doi.org/10.1007/978-3-319-25643-6_4.

Turnbull, J.C., Sweeney, C., Karion, A., Newberger, T., Lehman, S.J., Tans, P.P., Davis, K.J., Lauvaux, T., Miles, N.L., Richardson, S.J., Cambaliza, M.O., Shepson, P.B., Gurney, K., Patarasuk, R., Razlivanov, I., 2015. Toward quantification and source sector identification of fossil fuel CO_2 emissions from an urban area: Results from the INFLUX experiment. J. Geophys. Res.: Atmos. 120, 292–312. http://dx.doi.org/10.1002/2014JD022555.

Vaughan, A.R., Lee, J.D., Misztal, P.K., Metzger, S., Shaw, M.D., Lewis, A.C., Purvis, R.M., Carslaw, D.C., Goldstein, A.H., Hewitt, C.N., Davison, B., Beevers, S.D., Karl, T.G., 2016. Spatially resolved flux measurements of NO_x from London suggest significantly higher emissions than predicted by inventories. Faraday Discuss. 189, 455–472. http://dx.doi.org/10.1039/c5fd00170f.

Wilczak, J.M., Oncley, S.P., Stage, S.A., 2001. Sonic anemometer tilt correction algorithms. Bound.-Layer Meteorol. 99, 127–150. http://dx.doi.org/10.1023/A:1018966204465.

Wu, K., Davis, K.J., Miles, N.L., Richardson, S.J., Lauvaux, T., Sarmiento, D.P., Balashov, N.V., Keller, K., Turnbull, J., Gurney, K.R., Liang, J., Roest, G., 2022. Source decomposition of eddy-covariance CO_2 flux measurements for evaluating a high-resolution urban CO_2 emissions inventory. Env. Res. Lett. 17, 074035. http://dx.doi.org/10.1088/1748-9326/ac7c29.

Zavala, M., Huertas, J.I., Prato, D., Jazcilevich, A., Aguilar, A., Balam, M., Misra, C., Molina, L.T., 2017. Real-world emissions of in-use off-road vehicles in Mexico. J. Air Waste Manage. Assoc. 67, 958–972. http://dx.doi.org/10.1080/10962247.2017.1310677.